JGR Oceans

RESEARCH ARTICLE
10.1029/2020JC016922

Characteristics of 3-Dimensional Structure and Heat Budget of Mesoscale Eddies in the South Atlantic Ocean

Xue Wang[1,2], Shaoqing Zhang[1,2,3,4], Xiaopei Lin[1,2,3], Bo Qiu[1,5], and Lisan Yu[6]

[1]Key Laboratory of Physical Oceanography, Ministry of Education/Institute for Advanced Ocean Study/Frontiers Science Center for Deep Ocean Multispheres and Earth System (DOMES), Ocean University of China, Qingdao, China, [2]The College of Oceanic and Atmospheric Sciences, Ocean University of China, Qingdao, China, [3]Pilot National Laboratory for Marine Science and Technology (QNLM), Qingdao, China, [4]International Laboratory for High-Resolution Earth System Model and Prediction (iHESP), Qingdao, China, [5]Department of Oceanography, University of Hawaii at Manoa, Honolulu, HI, USA, [6]Department of Physical Oceanography, Woods Hole Oceanographic Institution, Woods Hole, MA, USA

Key Points:

- 3-dimensional structure of mesoscale eddies in the South Atlantic Ocean (SA) has been studied
- Two spatial patterns of mesoscale eddies in SA–dipole and monopole are identified
- Heat budget analysis reveals that meridional and vertical advections are the main factors that affect the formation of two types of the spatial patterns

Correspondence to:
S. Zhang and X. Lin,
szhang@ouc.edu.cn;
linxiaop@ouc.edu.cn

Citation:
Wang, X., Zhang, S., Lin, X., Qiu, B., & Yu, L. (2021). Characteristics of 3-dimensional structure and heat budget of mesoscale eddies in the South Atlantic Ocean. *Journal of Geophysical Research: Oceans*, *126*, e2020JC016922. https://doi.org/10.1029/2020JC016922

Received 19 NOV 2020
Accepted 22 APR 2021

Abstract Mesoscale eddies redistribute heat, salt, and nutrients in oceans. The South Atlantic Ocean (SA) is a basin that has active mesoscale eddies for which characteristics of the three-dimensional structure and its leading mechanism are complex but have yet been studied sufficiently. Here based on ocean reanalysis datasets we use a composite analysis approach to analyze the mixed layer anomalous heat budget and find distinct two types of spatial patterns: dipole and monopole – mainly present in the northern and southern regions of the SA, respectively. The dipole can be attributed to ocean horizontal advection, especially to the combined effect of eddy anomalous meridional current and meridional gradient of mean temperature. The monopole, on the other hand, is associated with complex contributions, for which zonal and meridional advections play opposite roles as cooling or heating around the eddies. At the eddy center, the vertical advection is non-negligible, especially the mean upwelling and vertical temperature gradient playing a vital role in the formation of a monopole. The analysis of eddy meridional heat transport shows that the stirring component is dominant, and poleward in most areas, especially at high latitudes. Such analysis on the leading mechanism of eddy-induced temperature anomaly could help improve our understanding on meso- and small-scale air-sea interactions and eddy-induced heat transport in the SA.

Plain Language Summary Mesoscale eddies can modulate the distribution of ocean heat content, and their imprint on temperature is dipole (monopole) in lower (higher) latitudes of the South Atlantic Ocean (SA). Here, applying the analysis of the mixed layer anomalous heat budget, we study the main mechanism of the spatial structure of the eddy-induced temperature anomaly in different regions of the SA. Results show that the meridional and vertical advections are the dominant factors that affect the formation of two types of the eddy structure patterns, and eddies with monopole structure can transport more heat poleward in the form of stirring.

1. Introduction

Mesoscale phenomena such as mesoscale eddies, with typical spatial scales of 50–300 km and temporal scales ranging from weeks to months, are prevalent in the world oceans. They carry huge kinetic energy (Chelton, Schlax, & Samelson, 2011; Ikeda et al., 1984), redistribute heat, salt and nutrients (Chelton, Gaube, et al., 2011; Ferrari & Wunsch, 2009; Qiu & Chen, 2005), and significantly affect ocean circulation and the overlying atmosphere dynamics (Chelton et al., 2004; Frenger et al., 2013; Gaube et al., 2015; Hausmann & Czaja, 2012; Villas Bôas et al., 2015). In general, generation of mesoscale eddies is spatially non-uniform, for example, large eddy variability usually appearing in regions such as the Kuroshio Extension (KE), the Subtropical Countercurrent (STCC), the Gulf Stream and the Antarctic Circumpolar Current (ACC) (Chaigneau et al., 2011; Hausmann & Czaja, 2012; Qiu & Chen, 2010; Yang et al., 2015). At present, using satellite altimeter observations, the general sea surface characteristics of mesoscale eddies, such as their geographical distributions, propagation tracks, rotational speeds, and lifetimes, have been studied frequently (Chelton, Schlax, & Samelson, 2011; Fu, 2006, 2009). In the past decade, the three-dimensional (3-D) structure of mesoscale eddies, particularly in the vertical aspect, which greatly controls their intensity,

endurance, and dissipation, has mostly been investigated in the northern hemisphere, for example, the Arabian Sea (de Marez et al., 2019), the South China Sea (Hu et al., 2011; Zhang et al., 2016), the KE region (Sun et al., 2017), and the North Atlantic subtropical gyre (Amores et al., 2017).

Although the South Atlantic Ocean (SA) is the smallest basin in the Southern Hemisphere, it possesses unique dynamic features and plays an important role in the global thermohaline circulation. As the link between the North Atlantic and the Southern Ocean (Garzoli & Matano, 2011), the SA gathers diverse water masses from different basins and presents complex temperature and salinity characteristics. In addition, the SA encompasses two energic regions, the Brazil-Malvinas confluence (BMC) and the Agulhas Current Retroflection (AGR), where instabilities are intense teeming with abundant mesoscale eddies (Downes et al., 2011; Jullion et al., 2010; Meijers et al., 2007; Sloyan & Rintoul, 2000; Villas Bôas et al., 2015).

Despite its importance, in-situ observations are sporadic and sparse in time and space in the SA (Garzoli et al., 2013; Garzoli & Matano, 2011). This makes it difficult to obtain a full picture of the mesoscale eddy distribution, not to mention their three-dimensional (3-D) structures. Advances in high-performance eddy-resolving numerical models now enable us to investigate the three-dimensional characteristics and mechanisms of SA eddies. Numerical simulations can provide much more information about eddy's 3-D structure than case studies using observations. For instance, by utilizing a 12 years (1996–2007) high-resolution numerical model product of oceanic circulation in the Southern California Bight, Dong et al. (2012) divide vertical shapes of eddies into three categories according to the position where the largest radius occurs: bowl-shaped eddies with the largest radius at the surface, lens-shaped eddies with the largest radius at the subsurface, and the cone-shaped eddies with the largest radius at the bottom. Waite et al. (2016) showed a wineglass shape down to 1,000 m based on the subsurface distribution of in-situ particles (particulate organic carbon, POC), leading to a sevenfold increase of vertical carbon flux in the eddy center versus the eddy flanks, which is called "wineglass effect." Thus, it is both feasible and desired to rely on the outputs of high-resolution numerical models in order to better understand the structure of mesoscale eddies in the SA.

Previous studies have mainly focused on the surface features of mesoscale eddies, and the three-dimensional structure of eddies in different regions in SA remains poorly known. Moreover, there is little knowledge about the quantitative mechanism analysis of eddy-induced temperature anomaly structures and the heat transports trapped by different types of eddies, which hinders a deep understanding of the dynamic processes of mesoscale eddies as well as the regional eddy-induced air-sea interactions. The objective of this study is to investigate the 3-D structures of oceanic eddies, attempting to reveal the leading mechanisms of the SA eddies with different temperature anomaly spatial structures, and discuss the impact of different types of mesoscale eddies on heat transport. In order to achieve this goal, we utilize the composite analysis and anomalous heat budget analysis for the mixed layer.

The paper is organized as follows. After the introduction, section 2 introduces the data and method used throughout this study. The composite analysis for the 3-D structure of mesoscale eddies is given in section 3, along with horizontal and vertical characterizations. In section 4, the leading mechanism of eddy-induced temperature anomalies spatial patterns is revealed by analyzing anomalous mixed layer heat budget, and the eddy-induced heat transport is discussed in section 5. Finally, summary and discussions are given in section 6.

2. Methodology

2.1. Data

The reanalysis data set from the Hybrid Coordinate Ocean Model (HYCOM) is obtained from the Naval Research Laboratory at Stennis Space Center, Mississippi, including salinity, potential temperature, sea surface height (SSH), and current velocity (eastward- and northward velocity). HYCOM is a primitive equation general ocean circulation model with a hybrid coordinate system which permits the model to simulate realistic ocean dynamics (Metzger et al., 2010, 2014; Bleck, 2002). The reanalysis uses the Navy Coupled Ocean Data Assimilation (NCODA) system for data assimilation, utilizing the model forecast as a first guess in a 3-D variational scheme and assimilating available satellite altimeter observations, in-situ Sea Surface Temperature (SST), in-situ vertical temperature and salinity profiles from XBTs, Argo floats and moored buoys (Cummings, 2005; Cummings & Smedstad, 2013). The horizontal resolution is 0.08° (~9 km) at the

equator and approximately 6.5 km at midlatitude, making it globally eddy-resolving for the mesoscale features that are addressed in this study. The hybrid coordinate system (that is isopycnal in the open stratified ocean, but smoothly transitions to z coordinates in the ocean mixed layer and sigma coordinates in coastal regions) has 41 layers vertically with potential density referenced to 2,000 m. The HYCOM reanalysis has been extensively validated and used in previous studies (e.g., Chen et al., 2017; Jensen et al., 2018; Luecke et al., 2017; Rydbeck et al., 2019; Trott et al., 2019).

2.2. Eddy Detection and Tracking Algorithm

In this study, we adopt an automated eddy detection method based on the geometry criterion proposed by Faghmous et al. (2015). Details of eddy detection are given as follows. The autonomous eddy identification algorithm starts to search for a single sea surface height anomaly (SSHA) extremum in locally defined pixels for a given SSHA snapshot. The extremum is defined as a grid cell whose SSHA is greater (maximum) or less (minimum) than its 8 neighbors in a 3×3 neighborhood. Once the eddy center is identified, the outermost closed contour of the SSH around the extrema is chosen as the eddy bound.

The eddy tracking algorithm used here is similar to that in Doglioli et al. (2007) and Chaigneau et al. (2008). The eddy amplitude is defined as the difference between the SSH at the eddy center and the mean SSH at the eddy bound. The radius of an eddy is defined to be the mean distance between the eddy center and the maximum geostrophic velocity. The rotational velocity is defined as the maximum geostrophic velocity computed along the eddy edge. This eddy detection and tracking scheme has been verified and widely applied to many regions (Escudier et al., 2016; Liu et al., 2020). Considering the data noise, eddies with radius smaller than 50 km or amplitude less than 3 cm are excluded.

2.3. Anomalous Heat Budget Analysis

The mixed layer heat budget represents the balance of various processes that contribute to the variability of the heat content in the upper ocean, and, consequently, affect the distribution of SST. The Mixed Layer Depth (MLD) is estimated as the depth at which the potential density difference from the 10 dbar value is equal to the threshold of the de Boyer Montégut et al. (2004):

$$\Delta_\sigma = \sigma\left(T_{10} - 0.2, S_{10}, P_0\right) - \sigma\left(T_{10}, S_{10}, P_0\right), \tag{1}$$

where T_{10} and S_{10} are temperature and salinity at 10 dbar and P_0 is sea surface pressure.

Usually, the heat budget in the oceanic mixed layer is expressed as (Giordani et al., 2013; Qiu et al., 2017; Qu, 2003; Stevenson & Niiler, 1983),

$$T_t = \frac{Q_{net}}{\rho C_p h} - \vec{v} \cdot \nabla T - \frac{w_e\left(T - T_{-h}\right)}{h} + \frac{Q_{diff}}{\rho C_p h}, \tag{2}$$

where T is the potential temperature vertically averaged over the mixed layer, the subscript t denotes time differential operator, and h is MLD. ρ is a reference density (1026 kg m^{-3}), C_p is the specific heat of seawater at constant pressure (3,986 J kg^{-1} K^{-1}), and Q_{net} represents the effective net surface heat flux retained within the mixed layer corrected for the penetrative shortwave radiation through the mixed layer base, specified by

$$Q_{net} = Q - Q_{pen}, \tag{3}$$

where Q is the net surface heat flux into the ocean, Q_{pen} is the shortwave radiation transmitted through the bottom of MLD, estimated by

$$Q_{pen} = Q_{short}\left[Re^{-h/\gamma_1} + \left(1 - R\right)e^{-h/\gamma_2}\right], \tag{4}$$

where R, γ_1, and γ_2 are coefficients that depend on water turbidity as classified by Jerlov (1968). For example, the Southern Ocean approximately falls into a water type with $R = 0.67$, $\gamma_1 = 1$, $\gamma_2 = 17$ (Dong et al., 2007; Huang et al., 2010).

The second term on the right-hand side of Equation 2 expresses the oceanic advection of heat composed by zonal advection and meridional advection. The horizontal velocity $\vec{v}$ is an average within the MLD.

The third term on the right-hand side of Equation 2 expresses the heat flux due to entrainment. w_e is the entrainment velocity across the base of the mixed layer, following the approach of Stevenson and Niiler (1983), we compute the entrainment velocity as in Ren and Riser (2009):

$$w_e = H\left(h_t + \vec{v}_{-h} \cdot \nabla h + w_{-h}\right) \tag{5}$$

where $\vec{v}_{-h}$ and $\vec{w}_{-h}$ are the horizontal and vertical velocity at the bottom of the mixed layer, respectively. h_t is the rate of change of the MLD. H is the Heaviside unit function $[H(x) = (1, x \geq 0 \; and \; 0, x < 0)]$. By this, only the entrainment (positive) velocity is considered to cool the mixed layer while the detrainment (negative) velocity plays no role. This is because the water that flows out from the base of the mixed layer has approximately the same characteristics as the water in the mixed layer and hence will not affect the temperature in the mixed layer (Nyadjro et al., 2012; Ren & Riser, 2009; Schlundt et al., 2014).

The last term on the right-hand side of Equation 2, Q_{diff}, is the vertical diffusive heat flux at the bottom of the mixed layer and is parameterized (Hayes et al., 1991) as

$$Q_{diff} = -\rho C_p \kappa \frac{\partial T}{\partial z} \tag{6}$$

Empirical studies (Jones, 1973; Robinson, 1966) indicate that the parameterizations of vertical eddy viscosity ν and eddy diffusivity κ take the following form:

$$\nu = \nu_c + \nu_0 \times \left(1 + \alpha R_i\right)^{-n} \tag{7}$$

$$\kappa = \kappa_c + \frac{\nu}{1 + \alpha R_i} \tag{8}$$

where the Richardson number R_i is:

$$R_i = \beta g \frac{\partial T}{\partial z} \times \left[\left(\partial u / \partial z\right)^2 + \left(\partial v / \partial z\right)^2\right]^{-1} \tag{9}$$

Here $\beta = 8.75 \times 10^{-6}\left(T + 9\right)\left(℃^{-1}\right)$ is the coefficient of thermal expansion of water, $g = 9.8\, m\, s^{-2}$ is the gravitational acceleration, ν_c and κ_c are background dissipation parameters, and ν_0, α and n are adjustable empirical parameters (Pacanowski & Philander, 1981). In this study, we assign constant values for these parameters as $\nu_0 = 3.5 \times 10^{-3}\, m^{-2}\, s^{-1}$, $\alpha = 5$, $n = 2$, $\nu_c = 1.0 \times 10^{-4}\, m^{-2}\, s^{-1}$, and $\kappa_c = 1.0 \times 10^{-5}\, m^{-2}\, s^{-1}$ as in Pacanowski and Philander (1981) and Timmermann and Beckmann (2004). Horizontal diffusion has been neglected owing to its small magnitude.

Following Zhang et al. (2007), the vertical entrainment is rewritten as

$$w_e \frac{T - T_{-h}}{h} \equiv -w_e \frac{\partial T}{\partial z}. \tag{10}$$

Equation 2 can be rewritten as

$$T_t = F \tag{11}$$

and

$$F = Q_q + Q_u + Q_v + Q_w + Q_{zz}, \tag{12}$$

where $T_t = \partial T / \partial t$ is referred to as potential temperature tendency and F as the forcing. The forcing is the sum of zonal advection: $Q_u = -u\partial T / \partial x$, meridional advection: $Q_v = -v\partial T / \partial y$, vertical entrainment: $Q_w = -w_e \partial T / \partial z$, adjusted surface heat flux: $Q_q = Q_{net} / \left(\rho C_p h\right)$, and vertical diffusion: $Q_{zz} = Q_{diff} / \left(\rho C_p h\right)$.

To detect the physical mechanism controlling the temperature distribution induced by mesoscale eddies in the South Atlantic Ocean, we apply a similar approach used in Huang et al. (2010). However, they studied ENSOs, low frequency tropical climate variability, and thus they first applied a low-pass filter (the cut-off period is mainly associated with tropical instability waves) to the original data, separating low- and high-frequency variations. Then they further decomposed heat budget equation into seasonal climatology and anomaly from seasonal mean. Here, we focus on mesoscale eddies whose lifetime is several months, relatively high frequent compared to ENSO. Thus, we directly use Reynolds decomposition to obtain climatology (bar) and anomaly mesoscale signals (prime). After this operation on Equations 11 and 12, the anomalous heat budget equation can be written as

$$T_t^{'} = Q_q^{'} + Q_u^{'} + Q_v^{'} + Q_w^{'} + Q_{zz}^{'}, \tag{13}$$

where

$$Q_q^{'} = Q_q - \overline{Q}_q \tag{14}$$

$$Q_u^{'} = -\overline{u}\frac{\partial T'}{\partial x} - u'\frac{\partial \overline{T}}{\partial x} - u'\frac{\partial T'}{\partial x} + \overline{u'\frac{\partial T'}{\partial x}} \tag{15}$$

$$Q_v^{'} = -\overline{v}\frac{\partial T'}{\partial y} - v'\frac{\partial \overline{T}}{\partial y} - v'\frac{\partial T'}{\partial y} + \overline{v'\frac{\partial T'}{\partial y}} \tag{16}$$

$$Q_w^{'} = -\overline{w}_e\frac{\partial T'}{\partial z} - w'_e\frac{\partial \overline{T}}{\partial y} - w'_e\frac{\partial T'}{\partial z} + \overline{w'_e\frac{\partial T'}{\partial z}} \tag{17}$$

The vertical diffusion

$$Q_{zz} = -\frac{\kappa}{h}\frac{\partial T}{\partial z}$$

is rewritten as $Q_{zz} = -\omega\partial T / \partial z$, where $\omega = K_z / h$ represents an equivalent entrainment velocity and can be decomposed into its climatology and anomaly: $\omega = \overline{\omega} + \omega'$, therefore,

$$Q_{zz}^{'} = -\overline{\omega}\frac{\partial T'}{\partial z} - \omega'\frac{\partial \overline{T}}{\partial z} - \omega'\frac{\partial T'}{\partial z} + \overline{\omega'\frac{\partial T'}{\partial z}}. \tag{18}$$

In our estimation of heat budget, the daily three-dimensional outputs of HYCOM are used. First, to separate the climatology and anomaly of signals, all variables are decomposed using the Reynolds decomposition in the entire SA domain. Then, we extract the regions within all identified eddies for the days according to the eddy position. Finally, we average all these snapshots to obtain a daily composite map. The same procedure is applied to the entire study period.

3. Characteristics of Mesoscale Eddies in the SA

3.1. Eddy Statistics

In the period of this study (2008–2018), 45,322 anticyclonic eddies (AEs) and 46,075 cyclonic eddies (CEs) are automatically identified and tracked using the SSH-based method developed by Faghmous et al. (2015) in the SA. The mean eddy properties are shown in Figure 1. Eddy frequency, which is defined as the

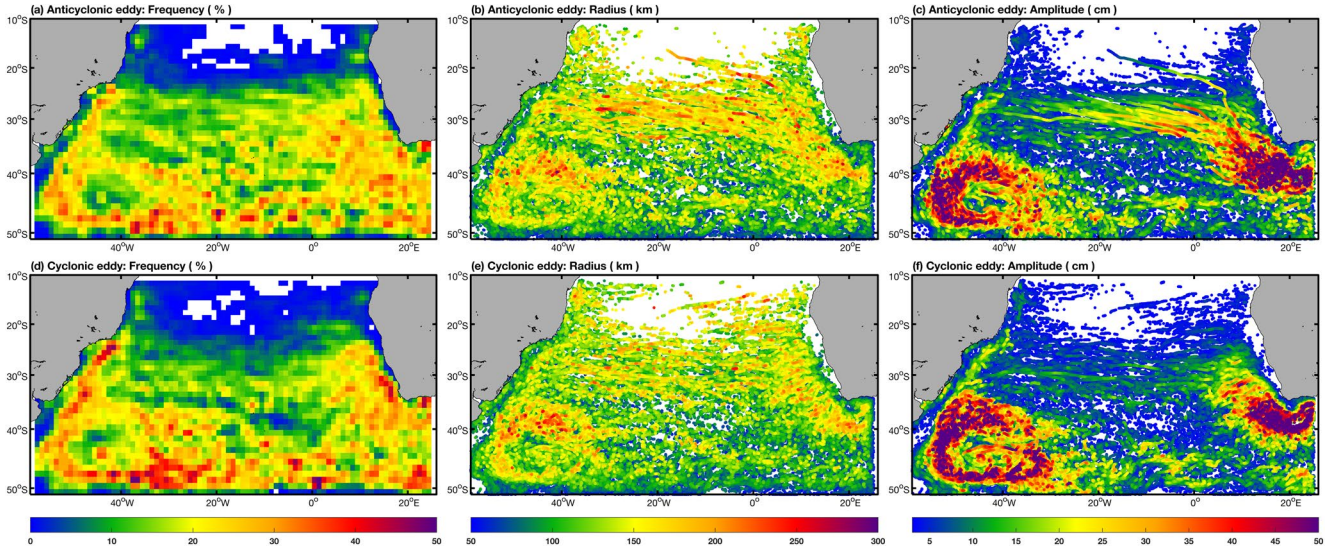

Figure 1. Spatial distribution of mean properties of mesoscale eddies detected and tracked using HYCOM data. (a) and (d) frequency (%), (b) and (e) radius (unit: km), and (c) and (f) amplitude (unit: cm) for AEs (top row) and CEs (bottom row). Mesoscale eddy frequency that represents the percentage of time in a 1° × 1° pixel in the South Atlantic Ocean during the whole time series. Eddies with radius, amplitude lower than 50 km, 3 cm are masked, respectively. AEs = anticyclonic eddies; CEs = cyclonic eddies.

percentage of time that each grid point was inside an eddy during the whole time series, for example, 100% represents that eddies are appearing all time at this area (Villas Bôas et al., 2015). As shown in Figures 1a and 1d, AEs and CEs are frequently observed south of ~30°S for the studied period, where the eddy frequency reaches from 20% to 50%. In contrast, eddy frequency drastically weakens in the subtropical SA between 10°S and 20°S, and is less than 5%. In general, the spatial distribution of cyclonic eddy frequency is in phase with anticyclonic eddy frequency in the SA, however, at Zapiola ridge, eddy frequency being higher than 40% for CEs and less than 10% for AEs.

Eddies in our study domain have a typical radius of around 50–300 km, varying largely with latitude with no significant difference with respect to eddy polarity. Large-radius (more than 180 km) eddies mainly distribute in the BMC and AGR (Figures 1b and 1e). Particularly, the radius of AEs is larger than CEs in the Agulhas eddies propagation corridor (anticyclonic Agulhas eddies) (see Figure 1b). In the work of Souza et al. (2011), they obtained a very similar geographical distribution of the eddies mean diameters resolved by the Wavelets and geometric criteria. Furthermore, they found that the eddies tracked through the geometric criteria present a relation between the diameter and the latitude very close to the curve of the first baroclinic mode Rossby deformation diameter.

The mean eddy amplitudes range between 3 and 50 cm, reflecting the strength extent of eddy kinetic energy (EKE) level. Likewise, the large-amplitude eddies mainly distribute in the BMC and AGR, corresponding to ~50 cm (Figures 1c and 1f). In addition, the observed amplitude of AEs is higher than CEs in the Agulhas eddies propagation corridor (see Figure 1c).

To avoid sporadic events, eddies with a duration shorter than 4 weeks are excluded. This led to 3,734 AE trajectories and 4,079 CEs trajectories for the 10 years analysis period. The spatial distribution of the eddy initial positions (birth locations) and the subsequent trajectories (colored by eddy lifespan) for AEs and CEs are shown in Figures 2a and 2b. It is evident that eddies with shorter lifetimes (<9 weeks) are randomly distributed, while eddies with longer lifetimes have a slight northwestward propagation pathway in the AGR and nearly westward pathway in the Agulhas eddies propagation corridor, and in the northern branch of the ACC, eddies with longer lifetimes have the meandering eastward migration pathway.

The eddy propagation velocity is estimated from the locations of the eddy centroids at consecutive time intervals along their trajectories (eddy drift velocity, $\bar{v}_d$) (Chelton, Schlax, & Samelson, 2011; Hausmann & Czaja, 2012). The estimates of averaged $\bar{v}_d$ for AEs and CEs within 2° × 2° boxes are shown in Figures 2c

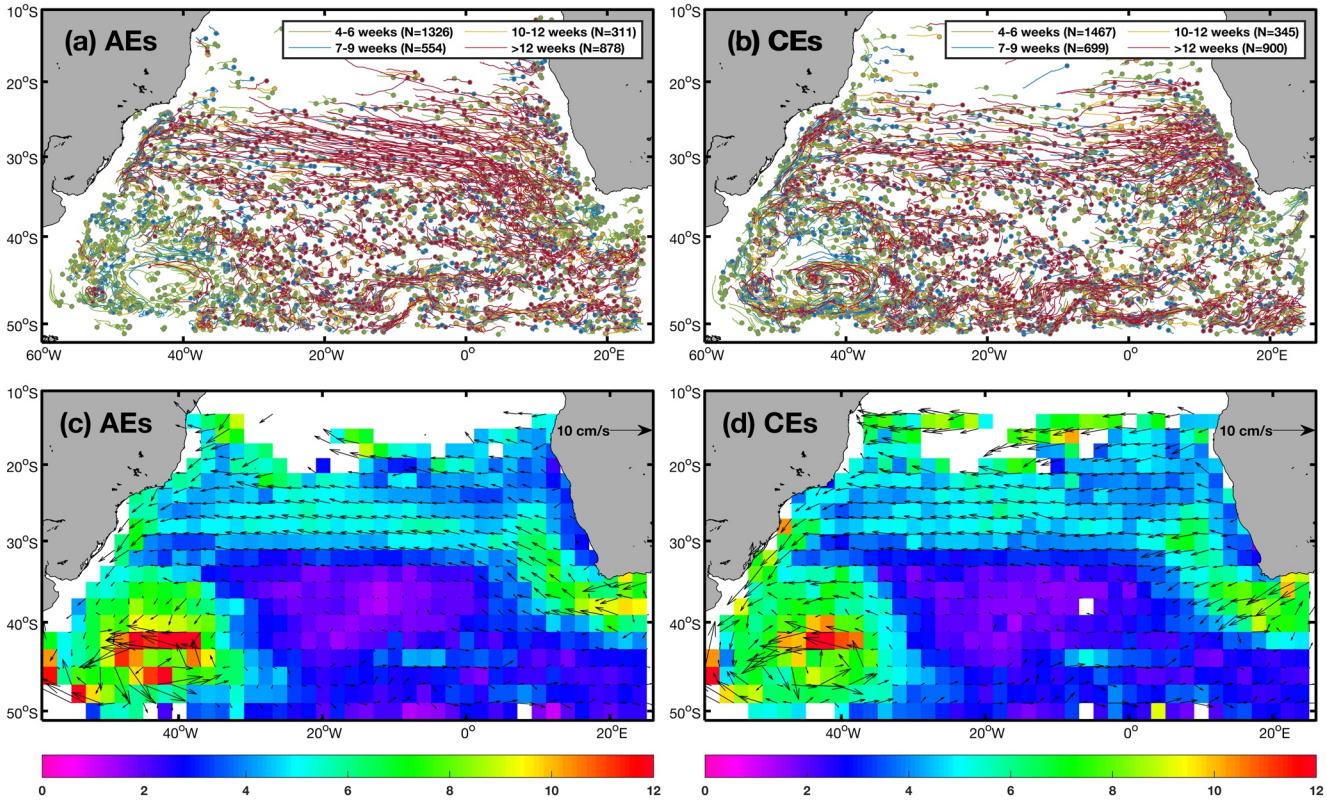

Figure 2. Eddy trajectories (top row) and eddy propagation velocity (bottom row; unit: cm/s) in the South Atlantic Ocean. Dots and colored lines in (a) and (b) denote birth positions of eddies and the propagation pathways, respectively. The arrows and color shading in (c) and (d) display the vector and the magnitude of eddy propagation velocity, respectively. A sample vector of 10 cm/s is shown at the top right corner.

and 2d. The arrows indicate the eddy propagation direction and the color shading displays the propagation speeds. The maximum occurs in the BMC, corresponding to 12 cm/s, while in the northern branch of the ACC, eddies with longer lifetimes have the eastward migration pathway. The eddies originated from the Agulhas Current region have the northwestward propagation velocities and a typical speed of 6–8 cm/s. After leaving the energetic source region, the eddies propagate westward along the Agulhas eddies propagation corridor. The similar result has also been found in the studies of Fu (2006) and (2009).

The EKE reflects an important aspect of the mesoscale ocean dynamics. EKE is defined by

$$EKE = \frac{1}{2}\left(u_g^{'2} + v_g^{'2}\right),$$

$$u_g^{'} = -\frac{g}{f}\left(\frac{\partial \mathrm{SLA}}{\partial \mathrm{y}}\right), v_g^{'} = \frac{g}{f}\left(\frac{\partial \mathrm{SLA}}{\partial \mathrm{x}}\right)$$

where f is the Coriolis parameter, g is gravity constant, $\vec{v}_g^{'}$ is the geostrophic velocity anomaly (also referred as eddy rotational velocity or eddy swirl velocity) derived from the surface level anomaly (*SLA*) data. The distribution of EKE calculated from the HYCOM outputs is shown in Figure 3. It is apparent that the largest EKE is present in BMC and AGR, and the weaker EKE is in the rest of the SA.

Similar to Souza et al. (2011), we first divide the South Atlantic Ocean into six sub-regions (see dashed boxes in Figure 3). These regions are (1) the interior of the Subtropical gyre, (2) the Brazil Current, (3) the Agulhas eddies corridor, (4) the AGR region, (5) the BMC, and (6) the northern branch of the ACC System. The geographical domains of the six sub-regions are presented in Table 1.

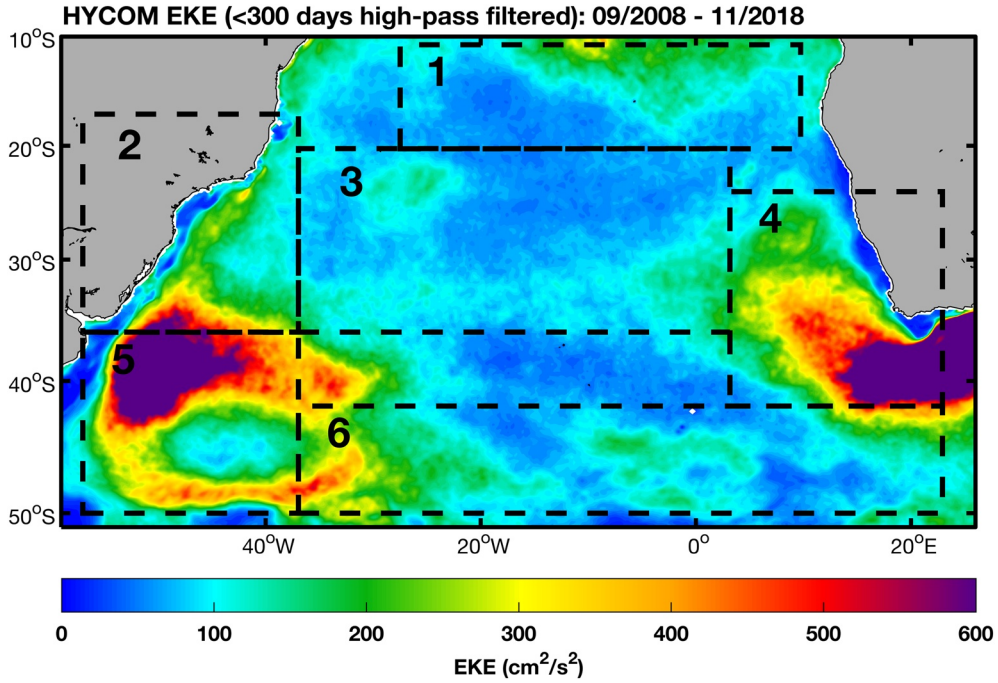

Figure 3. The distributions of Eddy Kinetic Energy (EKE) derived from HYCOM data during 2008–2018. Six areas of particular eddy dynamics are highlighted in dashed boxes: (1) the interior of the Subtropical gyre; (2) The Brazil Current; (3) the corridor of propagation of Agulhas Eddies; (4) The Agulhas Current retroflection region; (5) the Brazil-Malvinas confluence zone and (6) the northern branch of the Antarctic Circumpolar Current.

To extract eddy structure properties in different regions, we make use of normalized composite analysis. The procedure of this method is, for each identified AE or CE, the eddy fields are mapped onto a uniform grid of which the coordinates are normalized by the radius of each eddy, then averaged over all of the daily snapshots (Leyba et al., 2017; Souza et al., 2011; Villas Bôas et al., 2015; Zhan et al., 2019). The advantage of this technique is that averaging over many eddies as well as eddy trajectories helps suppress noise and reveal persistent eddy structures (Melnichenko et al., 2017).

Figures 4a and 4b shows the resulting horizontal composite structures of the eddy-induced SSHA and sea surface temperature anomalies (SSTA) for AEs and CEs, separately. The SSHA composites for all regions are showing that AEs (CEs) are prominently marked by a lifted (depressed) SSHA in the eddy center decreasing (increasing) toward the eddy edges.

The eddy-induced SSTA composite maps in the interior of the Subtropical gyre (region 1) exhibit a dipole pattern with week amplitudes of about ±0.3℃. In regions 2 and 3, the SSTA induced by eddies shows a clear asymmetrical dipole pattern, and the asymmetry is manifested in two aspects. One is position asymmetry: warm (cold) eddies are north-south (east-west) asymmetry, the warm pole is distributed on the south (east)

Table 1
Limits Between Regions in the South Atlantic Ocean

Region	Latitude limits	Longitude limits	Mean dynamic feature
1	10°S–20°S	30°W–10°E	Subtropical gyre
2	18°S–36°S	60°W–40°W	Brazil Current
3	20°S–36°S	40°W–0°	Agulhas Eddies propagation corridor
4	24°S–42°S	0°—20°E	Agulhas Current retroflection
5	36°S–50°S	60°W–40°W	Brazil-Malvinas Confluence Zone
6	42°S–50°S	40°W–20°E	Antarctic Circumpolar Current

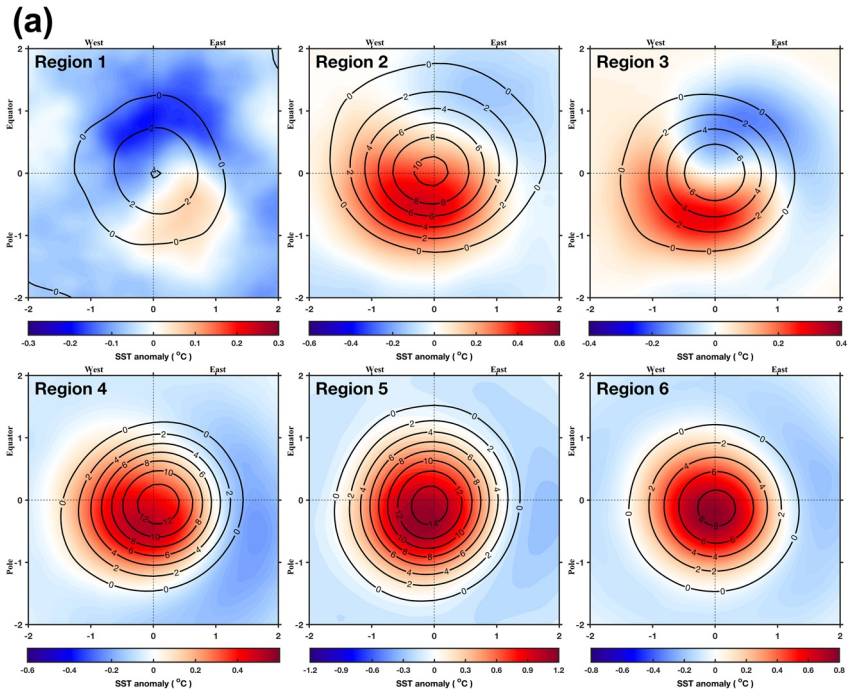

Figure 4a. Climatological averaged composite maps of anomalies of SSH (contours; unit: cm), SST (color; unit: ℃) inside AEs in 6 sub-regions of the South Atlantic Ocean. The axes in the composite maps are normalized by the individual eddy radius. SSH = sea surface height; SST = sea surface temperature. C.I. is 2 cm.

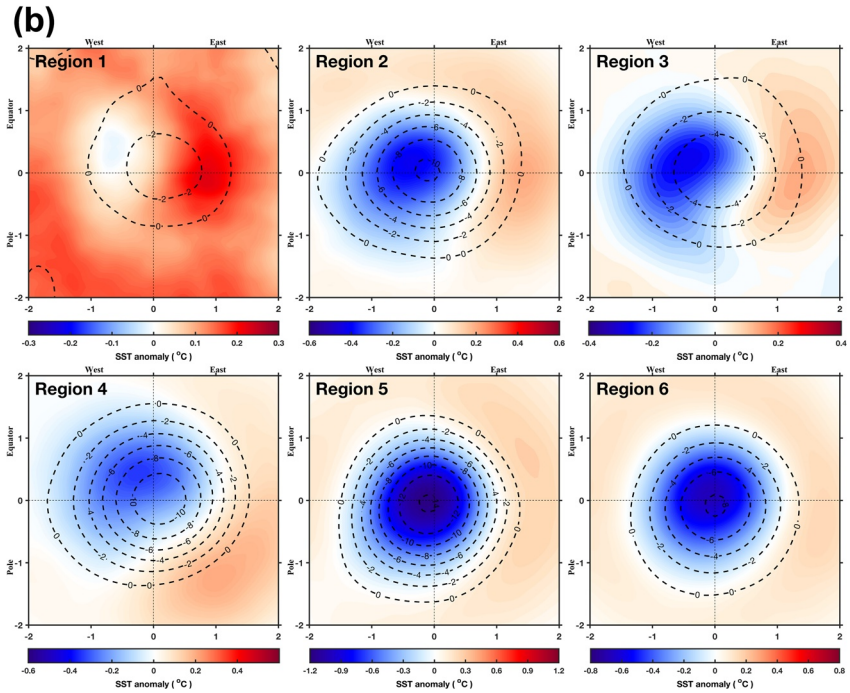

Figure 4b. The same as Figure 4a, except for CEs (dashed for negative).

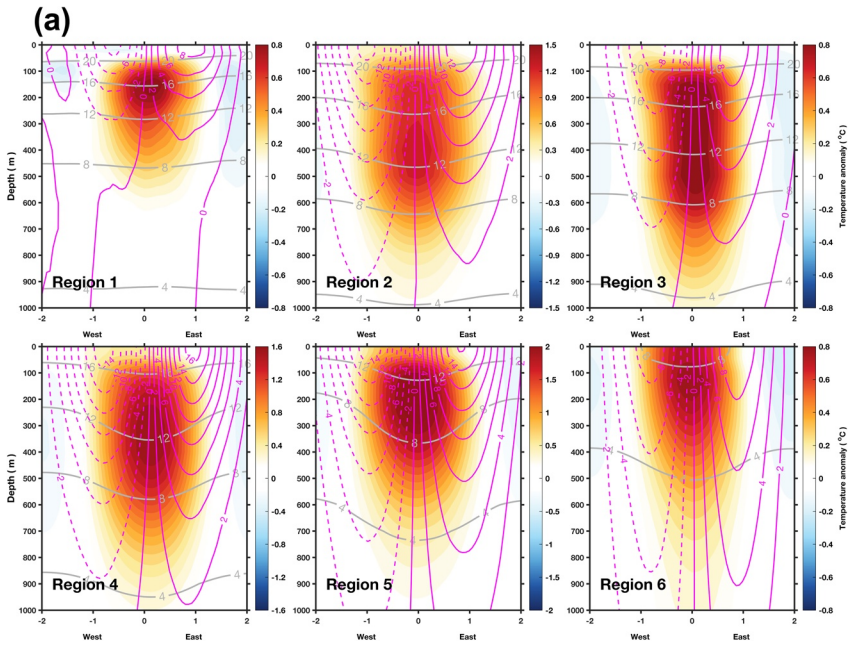

Figure 5a. Composite zonal sections of vertical structure across AEs in six sub-regions of the South Atlantic Ocean. The composite mean potential temperature (unit: ℃), positive meridional (northward) velocity (unit: cm/s), negative meridional (southward) velocity, and temperature anomaly (unit: ℃), are depicted with gray contours, magenta solid contours, magenta dashed contours, and color shading, respectively.

side of the composite area, and the cold poles are distributed on the north side (west) of the composite area, which has a tongue-like shape surrounding the eddy center; the second is the asymmetry of the polar intensity: the warm (cold) pole of AEs (CEs) is slightly stronger than the cold (warm) one. The same dipole signature of mesoscale eddies by analyzing the relationship between satellite sea surface salinity (SSS) and SSH variability has also been found in the study of Melnichenko et al. (2017) in the southern Indian Ocean (65°E–105°E, 15°S–30°S) and the North Atlantic subtropical gyre region (45°W–25°W, 17°N–23°N; 45°W%–25°W, 26°N–32°N). Liu et al. (2020) point out that the dipole structure of the South China Sea is related to the sign consistency between SST and SSH and only 56% of AEs are correspond to positive SSTA and 58% of CEs to negative SSTA.

In regions 4, 5, and 6, the SSTA induced by eddies shows a monopole pattern, SSHA and SSTA have a relatively in-phase relationship no matter in a high level of eddy activity regions (such as AGR and BMC) or weaker EKE zone (the northern branch of the ACC). A closer inspection of these regions reveals that the eddy-induced maximum SST anomalies are not centered on the eddy cores but slightly shifted pole- and westward over AEs, and over CEs, slightly equator- and westward.

3.2. Three-Dimensional Structures

In order to illustrate the shapes of mesoscale eddies, Figures 5 and 6 present the vertical composite maps of eddy-indued anomalies in the study regions. Figure 5 shows vertical sections crossing the composite eddy center of the zonal section of mean temperature (gray contours), temperature anomalies (in color), northward velocity (magenta solid contours), and southward velocity (magenta dashed contours) for AEs (Figure 5a) and CEs (Figure 5b). We note that in the eddy core of the composite eddies, mean maximum anomalies appear in different depths of subsurface in the six sub-regions of the SA. For AEs (CEs), the maximum temperature anomaly is up to 2.0℃ at around 200 m found in the BMC region (region 5). The composite AEs have an anticlockwise rotational velocity distribution accompanied by a depression of the isotherm whose slope increases with depth, while the composite CEs have a clockwise rotational velocity distribution with the isotherm contours' doming toward the CE center.

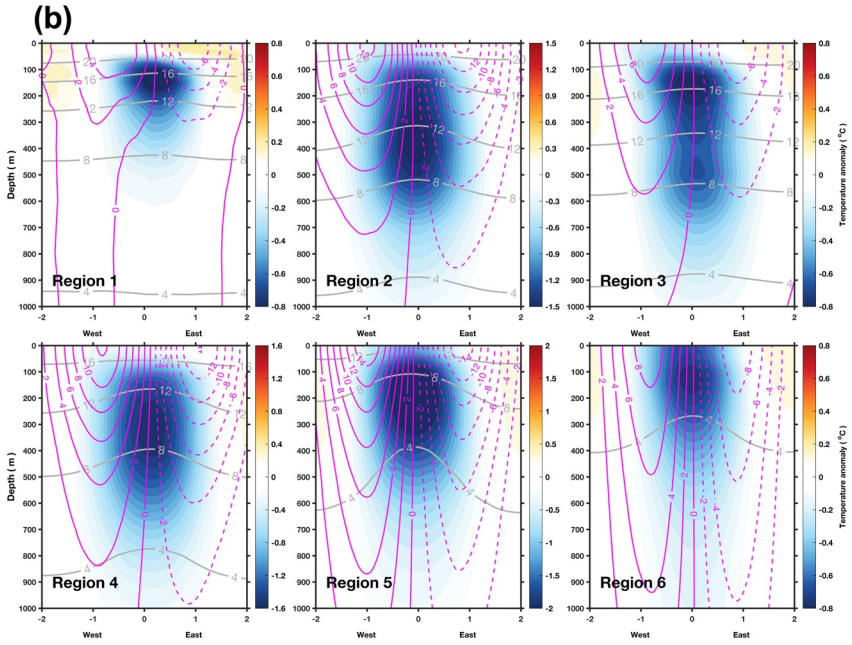

Figure 5b. The same as Figure 5a, except for CEs.

It is noticeable that the structures of meridional (zonal) velocity anomalies in region 1 (the interior of the Subtropical gyre) and region 3 (Agulhas Eddies propagation corridor) tilt slightly westward (southward) from surface to the depth below 1,000 m (the structures of zonal velocity anomalies are not shown). Similar tilting features in the velocity structures are also reported in the previous work by Zhang et al. (2016). While they pointed out that the topographic β effect is likely the cause for the observed vertically tilting structures, especially in the marginal seas with broad-scale continental slopes. Thus, the underlying mechanism of the tilted 3-D structures in the open oceans require further investigation.

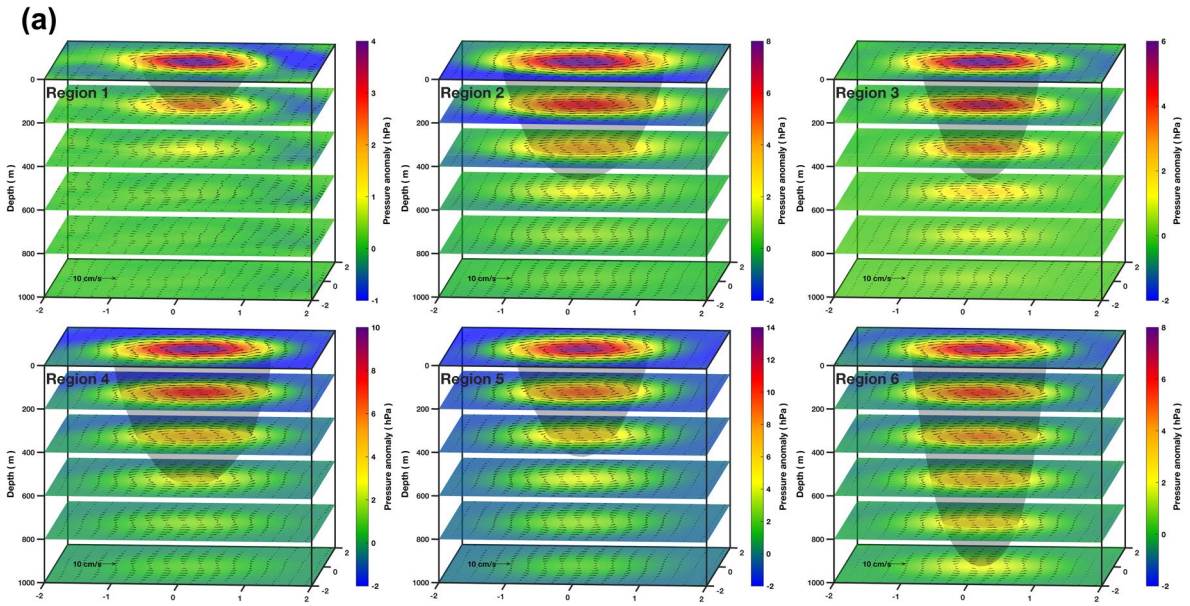

Figure 6a. Composite eddy 3-D structures of anomalies of seawater pressure (color; unit: hPa), black vectors indicate eddy rotational velocity anomaly (unit: cm/s) inside AEs in 6 sub-regions of the South Atlantic Ocean. The *x*, *y* axes in the composite maps are normalized by the individual eddy radius. A sample vector of 10 cm/s is shown at the bottom left corner.

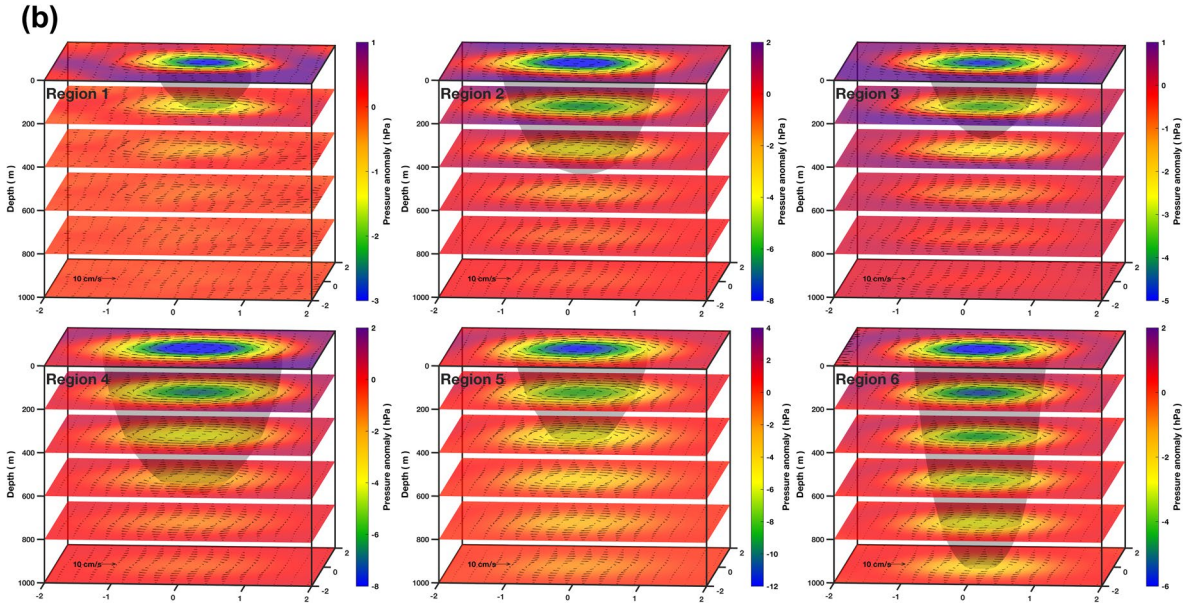

Figure 6b. The same as Figure 6a, except for CEs.

Figure 6 shows the 3-D composites of seawater pressure anomalies (in colors) and geostrophic velocity anomalies (in arrows) induced by eddies. Vertically, eddy pressure anomalies are surface-intensified, with velocity sharply decreasing with depth. The average eddy shape is like a bowl with largest radius at the surface and there is no significant difference for AEs (Figure 6a) and CEs (Figure 6b). Again, the composite eddy edges reach in different depths in the six SA sub-regions (also see Figure 13). The observed maximum of thickness in region 6 (the northern branch of the ACC) can reach to 1,000m, whereas in the interior of the Subtropical gyre it is only about 200 m. The vertical extent of the trapped fluid that is effectively transported by eddies will be discussed more in section 5.

4. Analysis of Leading Mechanism

Before utilizing the mixed layer anomalous heat budget, it is necessary to address if a reasonable closure of the temperature budget is maintained. To demonstrate the closure of the mixed layer anomalous heat budget, the correlation coefficient between T_t and forcing ($Q_q + Q_u + Q_v + Q_w + Q_{zz}$) is calculated using a daily temperature budget of 10 years. Figure 7 shows that the correlation coefficient is above 0.92 in all sub-regions of the SA. Some inconsistencies in these curves may be associated with the defects of the parameterization of vertical entrainment and diffusion. The good closure (Figure 7) indicates that the anomalous temperature budget described by Equation 13 ensures that the results regarding the leading mechanisms of eddy's spatial structure are robust.

In order to investigate the leading mechanism which determines the two spatial patterns of eddy-induced SST anomalies, the mixed layer anomalous heat budget analysis is carried out for the northern ($10^{\circ}S$–$30^{\circ}S$) and southern ($30^{\circ}S$–$50^{\circ}S$) regions of the study domain.

4.1. In Northern Regions

The various forcing terms for the tendency of mixed layer anomalous temperature in northern regions ($10^{\circ}S$–$30^{\circ}S$) are shown in Figure 8. The composite anomalous temperature tendency $\left(T_t\right)$ (see Figure 8a) of the mixed layer caused by CEs presents a relatively symmetrical dipole pattern, with a negative anomaly of $-0.15\,℃\,mon^{-1}$, a positive anomaly of $0.20\,℃\,mon^{-1}$ in the western and eastern side of composite area, respectively. The composite distribution of the adjusted surface net flux $\left(Q_q\right)$ (see Figure 8b) is also a dipole pattern with its warm pole slightly larger than the cold one, which is out of phase with T_t, showing a weaker

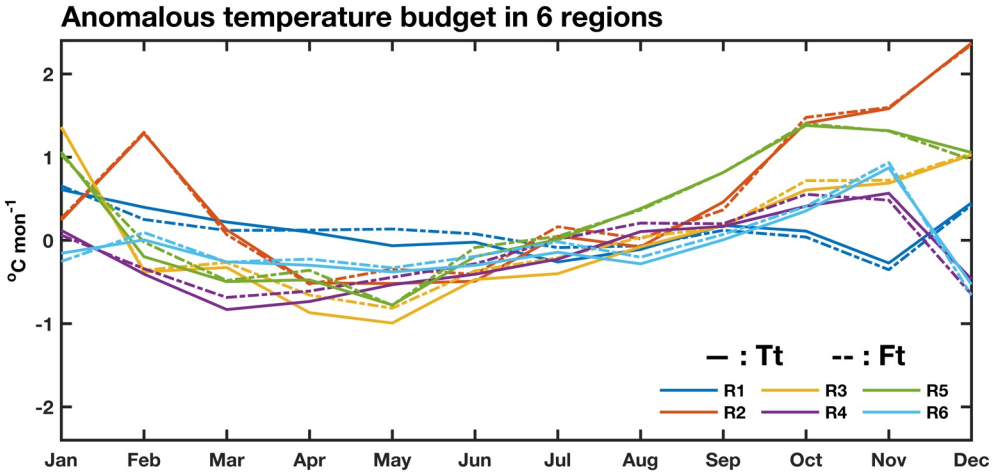

Figure 7. Climatological (year 2008–2018) anomalous temperature budget closure in six sub-regions of the South Atlantic Ocean. The correlation coefficients between T_t and the forcing ($F_t = Q_q + Q_u + Q_v + Q_w + Q_{zz}$) are 0.9192, 0.9970, 0.9967, 0.9659, 0.9965, and 0.9825, individually.

damping effect on T_t. The horizontal advection term ($Q_u + Q_v$) (see Figure 8c) is basically consistent with the T_t, indicating that $Q_u + Q_v$ is the dominant term in the mixed layer anomalous temperature budget equation and plays a leading role in the structure formation of T_t within CEs. The combination term of entrainment and vertical diffusion ($Q_w + Q_{zz}$; hereafter as vertical advection) (see Figure 8d) is a uniform negative anomaly in the entire eddy composite area. Considering that $Q_w + Q_{zz}$ is one order of magnitude smaller than T_t, so vertical advection has little effect on the anomalous temperature tendency.

To gain further insights, we decompose the forcing terms of the mixed layer temperature tendency along a chord through the center of CEs from the west to east of the composite area (Figure 9**)**. The total temperature tendency (T_t in Figure 9a denoted by a black line) represents the HYCOM change in daily temperature and contains all components of the anomalous temperature Equation 13. The largest component is horizontal advection ($Q_u + Q_v$), especially meridional advection, varying consistently with T_t and the maximum existing at the 1-time normalized standard eddy radius whereas around the eddy center having the minimum, indicating there is a dipole pattern. For meridional advection, we can see that the combined effects ($-v' \cdot \overline{T}_y$ denoted by a green line in Figure 9c) of the anomalous meridional current and the meridional gradient of mean temperature contribute to the dipole structure of low latitude CEs. The heat flux forcing term is smaller and varies out of phase with temperature tendency, acting mainly to cool (warm) the mixed layer temperature east (west) of the composite eddy center. The combination term of entrainment and vertical diffusion ($Q_w + Q_{zz}$ denoted by a cyan line in Figure 9a) is notably weaker than other forcing terms, indicating that it plays an insignificant role in the dipole structure of CEs in northern regions of the SA.

4.2. In Southern Regions

The anomalous temperature tendency $\left(T_t\right)$ (Figure 10a) of the mixed layer caused by CEs is an asymmetric dipole pattern in southern regions ($30^\circ S$–$50^\circ S$) of the SA. The negative anomaly ($-0.20\,℃\,mon^{-1}$) west of the composite area is larger and the positive anomaly ($0.10\,℃\,mon^{-1}$) on the east has a smaller range. The composition of sea surface net flux (Q_q) (Figure 10b) has a dipole pattern, the maximum around the eddy center is $0.12\,℃\,mon^{-1}$, and the warm center is slightly shifted westward. The magnitude of Q_q is equivalent to T_t, that is, the downward (positive) heat flux within the domain of a standard normalized eddy radius is mainly used to heat the surface temperature. The magnitude of horizontal advection term (Figure 10c) is about two times bigger than T_t, indicating that the horizontal advection is the dominant term in the mixed layer anomalous temperature budget equation. The vertical advection (Figure 10d) has a dipole pattern, and it has a same magnitude with T_t, which shows that the vertical advection plays a critical role on the spatial pattern of eddy-induced temperature anomalies.

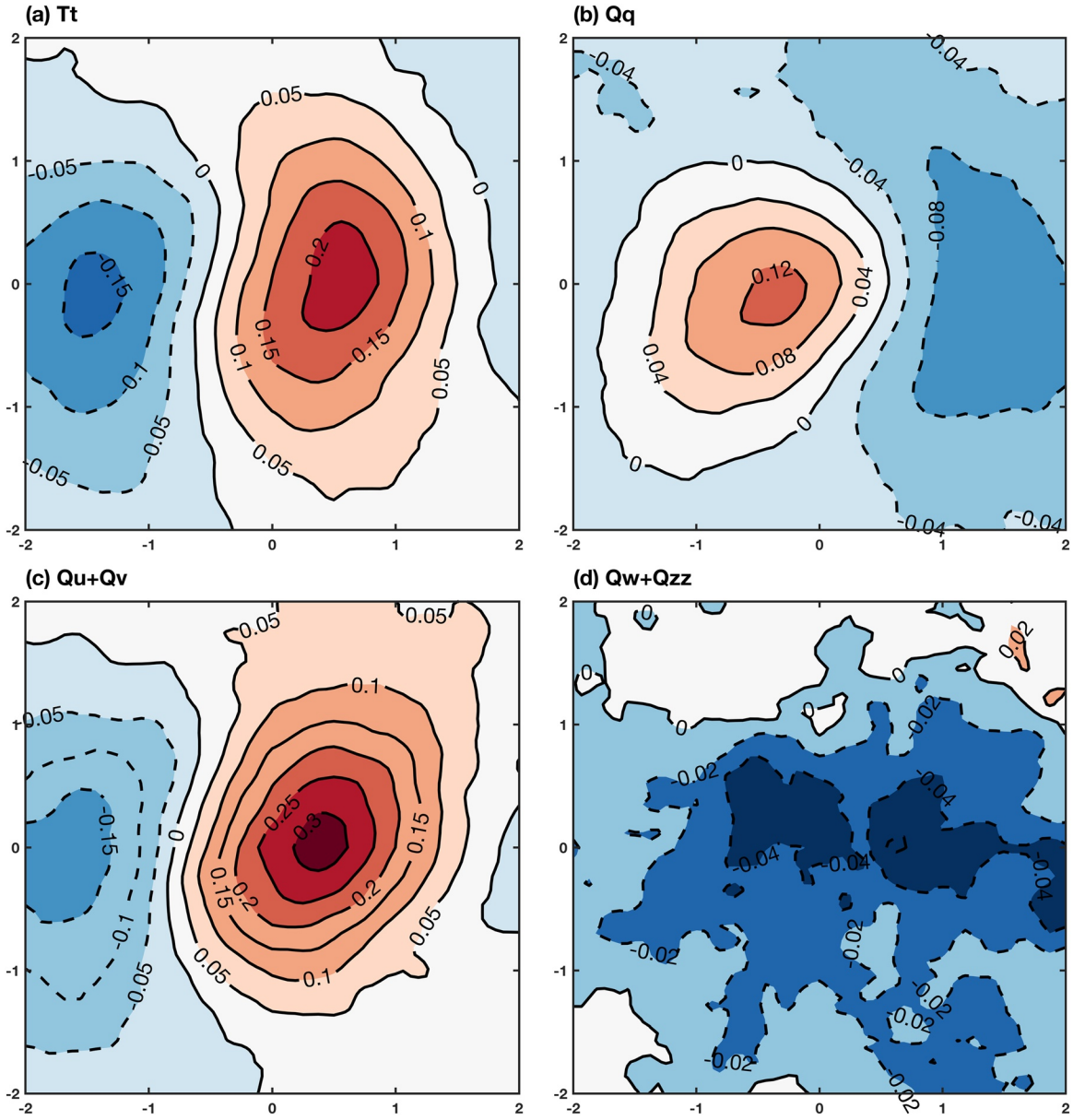

Figure 8. Anomalous temperature budgets (dashed contours for negative; unit: ℃ mon^{-1}) of CEs composite in northern regions (10°S–30°S) of the SA by (a) Temperature tendency (T_t), (b) Net surface heat flux $\left(Q_q\right)$, (c) Zonal and Meridional advection ($Q_u + Q_v$), and (d) Entrainment and vertical diffusion ($Q_w + Q_{zz}$). (c)I. is 0.05 ℃ mon^{-1} in (a) and (c), 0.04 ℃ mon^{-1} in (b), and 0.02 ℃ mon^{-1} in (d).

The decomposition of heat budget and more detailed look at each variable are shown in Figures 11 and 12, respectively. The decomposition shows that the spatial structure of zonal advective heating and cooling result from combined effects ($-\overline{u} \cdot T_x^{'}$ in Figures 11b denoted by a red line) of the zonal gradient of anomalous ($T_x^{'}$ in Figure 12d) mixed layer temperature, as well as the sign of mean ($\overline{u}$ in Figure 12g) zonal current of the mixed layer. The sign of the zonal gradient of anomalous temperature is opposite west and east of the eddy center, while the sign of mean zonal current is uniform in the entire composite area. That is why the combined zonal advection by mean zonal current contributes to a warming (cooling) west (east) of the eddy center.

The role of meridional advection is mainly on anomalous advection ($-v' \cdot \overline{T}_y$ in Figure 11c denoted by a green line). Further analysis confirms that the anomalous advection is directly associated with the strong

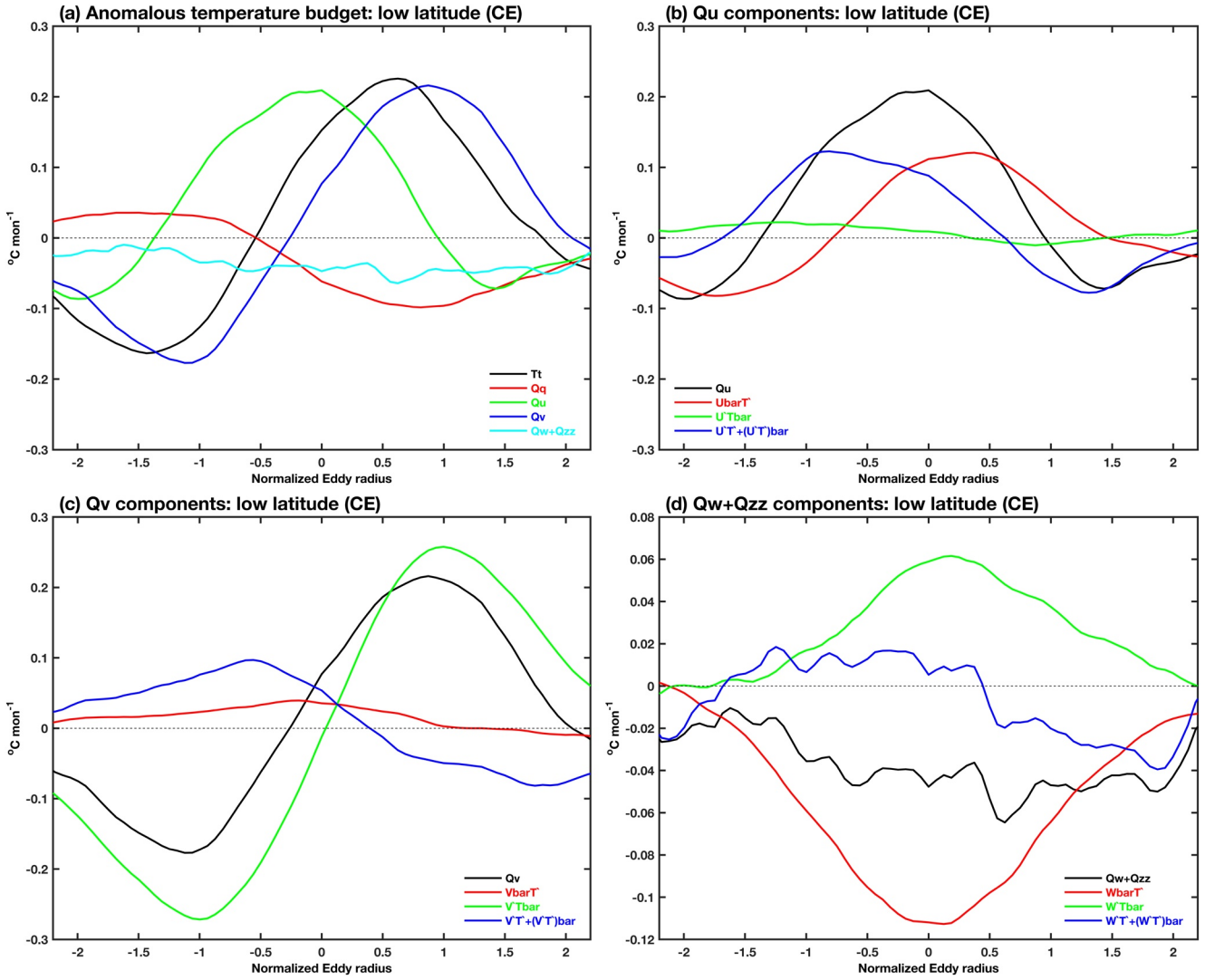

Figure 9. Temperature budget anomalies of CEs in northern regions ($10^{\circ}S$–$30^{\circ}S$) of the SA along a chord through the eddy center from west to east of the composite area. (a) Anomalous temperature budgets (℃ mon^{-1}). Decomposition of (b) Zonal advection, (c) Meridional advection, and (d) Entrainment and vertical diffusion. Decomposed climatology and associated anomaly are noted as bar and prime, for example $\overline{U}T' = -\overline{u} \cdot T_x'$. The terms such as $U'T' = -u' \cdot T_x'$ represents the non-linearity.

meridional gradient of mean ($\overline{T}_y$ in Figure 12b) temperature and large anomalous (v' in Figure 12k) meridional current. The meridional gradient of mean temperature is uniform in the entire composite area, while the sign of anomalous meridional current is opposite west and east of the eddy center. Therefore, the combined meridional advection by anomalous meridional current contributes to a cooling (heating) west (east) of the eddy center.

Although horizontal advection terms are larger than other forcing terms (Figure 11a), they play the opposite role on the formation of eddy composite structure and mainly affect the area around the 1-time normalized standard eddy radius. However, within a standard normalized eddy radius, especially around the eddy center, the zonal and meridional advection cancel out each other while the vertical advection cannot be neglected. The components of vertical advection show that mean ($-\overline{w} \cdot T_z'$ in Figure 11d denoted by a red line) and anomalous ($-w' \cdot \overline{T}_z$ in Figure 11d denoted by a green line) vertical current contribute about equally to the monopole pattern. The former process associates with the weaker vertical gradient of anomalous temperature (T_z' in Figure 12f) and the stronger mean ($\overline{w}$ in Figure 12i) upwelling, therefore the combined result

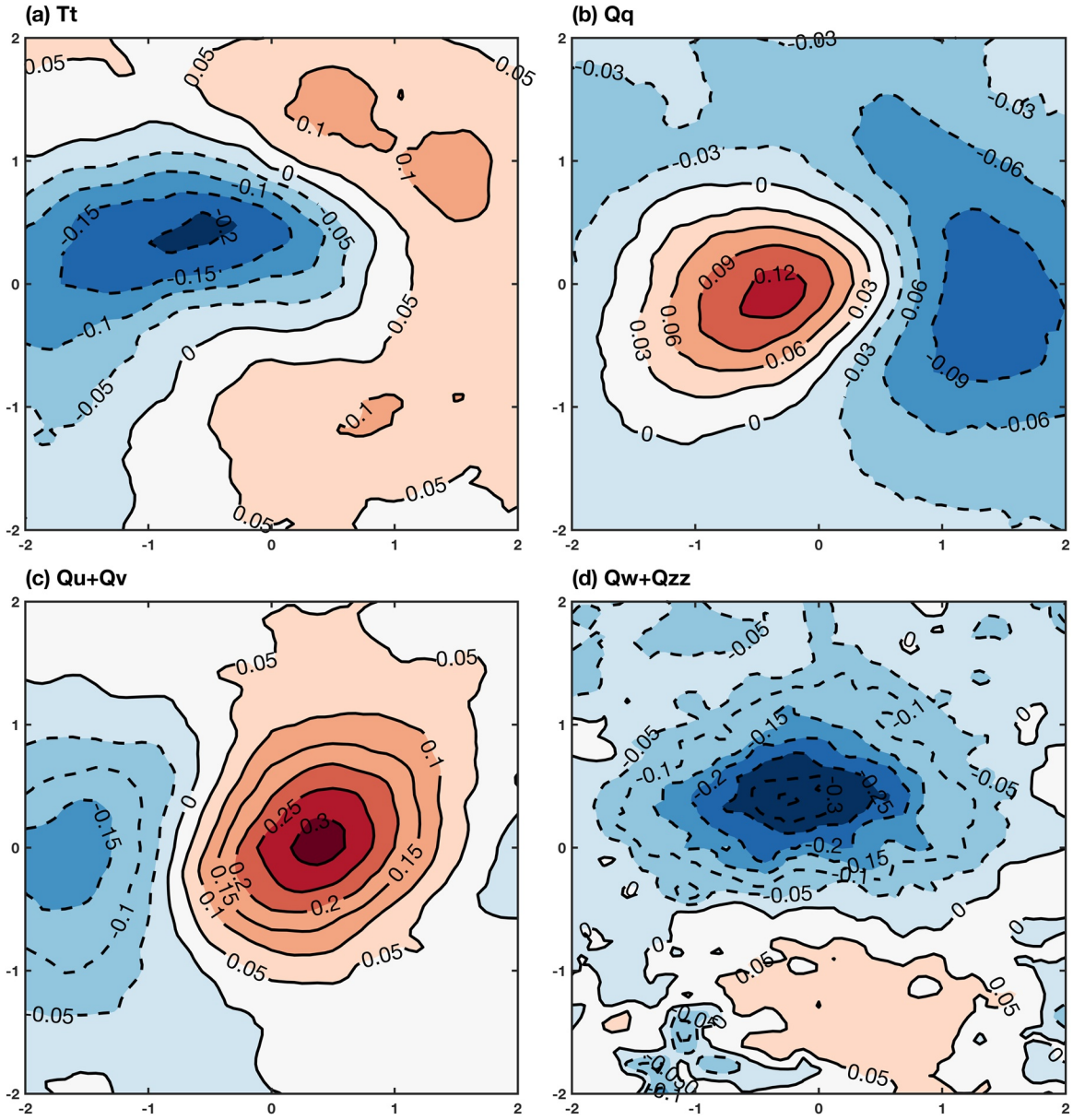

Figure 10. Anomalous temperature budgets (dashed contours for negative; unit: ℃ mon^{-1}) of CEs composite in southern regions (30°S–50°S) of the SA by (a) Temperature tendency (T_t), (b) Net surface heat flux $\left(Q_q\right)$, (c) Zonal and Meridional advection ($Q_u + Q_v$), and (d) Entrainment and vertical diffusion ($Q_w + Q_{zz}$). (c)I. is 0.05 ℃ mon^{-1} in (a), (c), and (d), and 0.03 ℃ mon^{-1} in (b).

is a cooling effect. The latter process associated with the stronger vertical gradient of mean temperature ($\overline{T}_z$ in Figure 12c) and the weaker anomalous (w' in Figure 12l) downwelling contributes heating effect. In addition, the non-linear ($-w' \cdot T'_z$ in Figures 11d denoted by a blue line) term also contributes a weaker heating effect. As a whole, the mean upwelling and vertical temperature gradient in an eddy center play a more important role in the formation of the monopole structure.

5. Eddy-Induced Heat Transport

The most thrilling feature of mesoscale eddies is that they are capable to transport water properties such as heat, salt, and potential vorticity, as well as biogeochemical characteristics (Chelton, Schlax, & Samelson, 2011; Frenger et al., 2018; Hausmann & Czaja, 2012; Sun et al., 2019; Yang et al., 2015; Zhan et al., 2019;

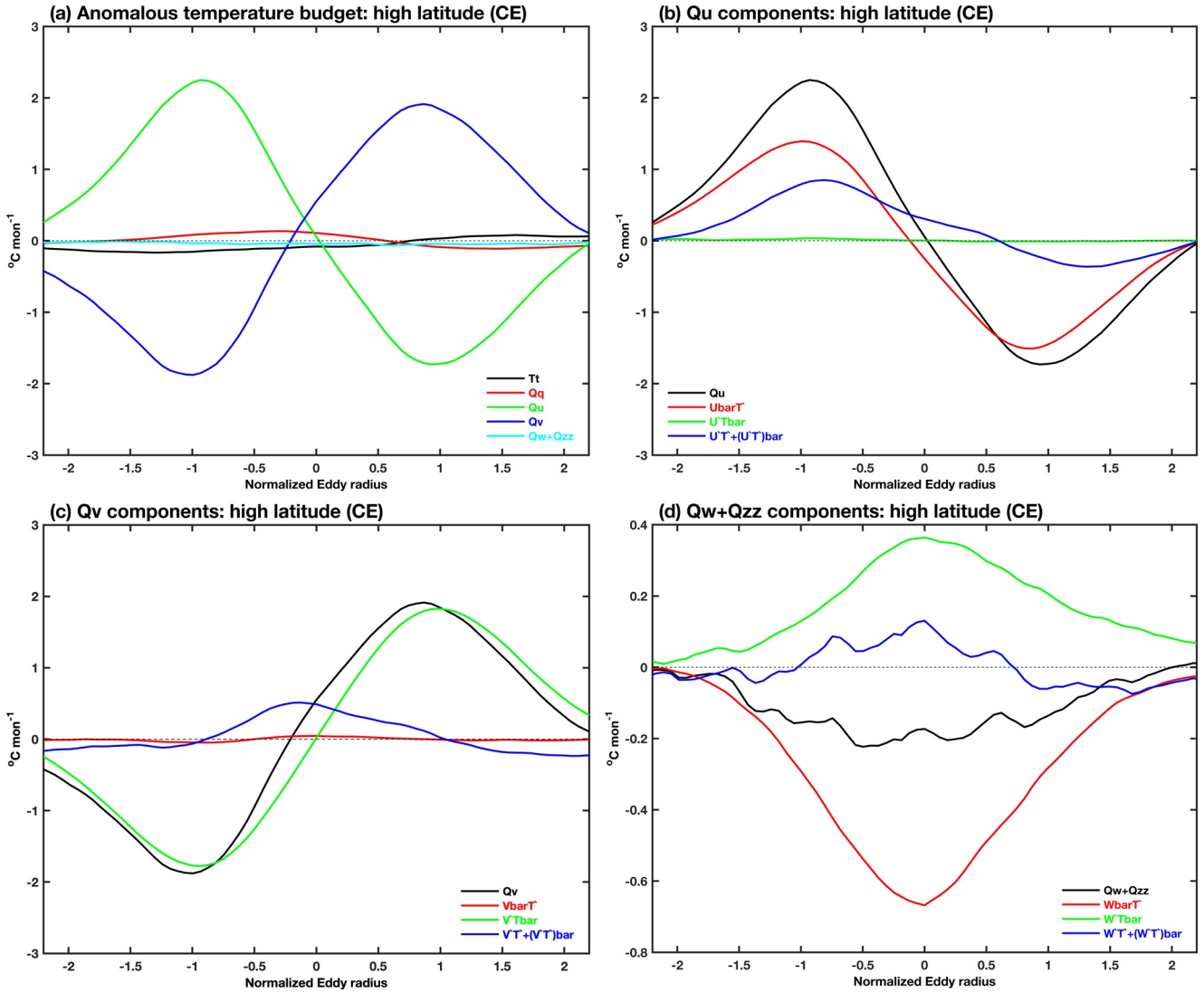

Figure 11. Same as Figure 9 except for temperature budget anomalies of CEs at high latitude (30°S–50°S) along a chord through the eddy center from west to east of the composite area.

Zhang et al., 2014). To estimate the water amount effectively trapped and transported by the eddies, we utilize the concept of trapping depth (Flierl, 1981; Chaigneau et al., 2011), which depends on the ratio of the eddy swirl velocity (geostrophic velocity anomaly) to the eddy drift velocity (see Figures 2c and 2d), called the nonlinearity parameter. More generally, the value of the ratio that exceeds one implies that there is trapped water within the eddy interior that is advected with the eddy as the eddy translates (Chelton, Schlax, & Samelson, 2011). Figure 13 shows the vertical extent of the trapped water in the composite of AEs and CEs in 6 sub-regions of the SA. The trapping depth is smallest in the region 1 (the interior of the Subtropical gyre; see Figure 13a) and largest in the region 6 (the northern branch of the ACC; see Figure 13f). These values correspond to 200 m and 1,100 m, respectively.

The heat transport induced by mesoscale eddies can be attributed by two processes. One is swirling heat transport (stirring component) relating to the eddy rotational velocity ($\vec{v}_g'$), and the other one (trapping component) is drifting heat transport due to eddy movements (with drift velocity, $\vec{v}_d$) (Amores et al., 2017; Hausmann & Czaja, 2012; Zhan et al., 2019). Following previous studies, the eddy-induced heat transports across an individual eddy at a certain depth z (unit: W/m) are estimated as:

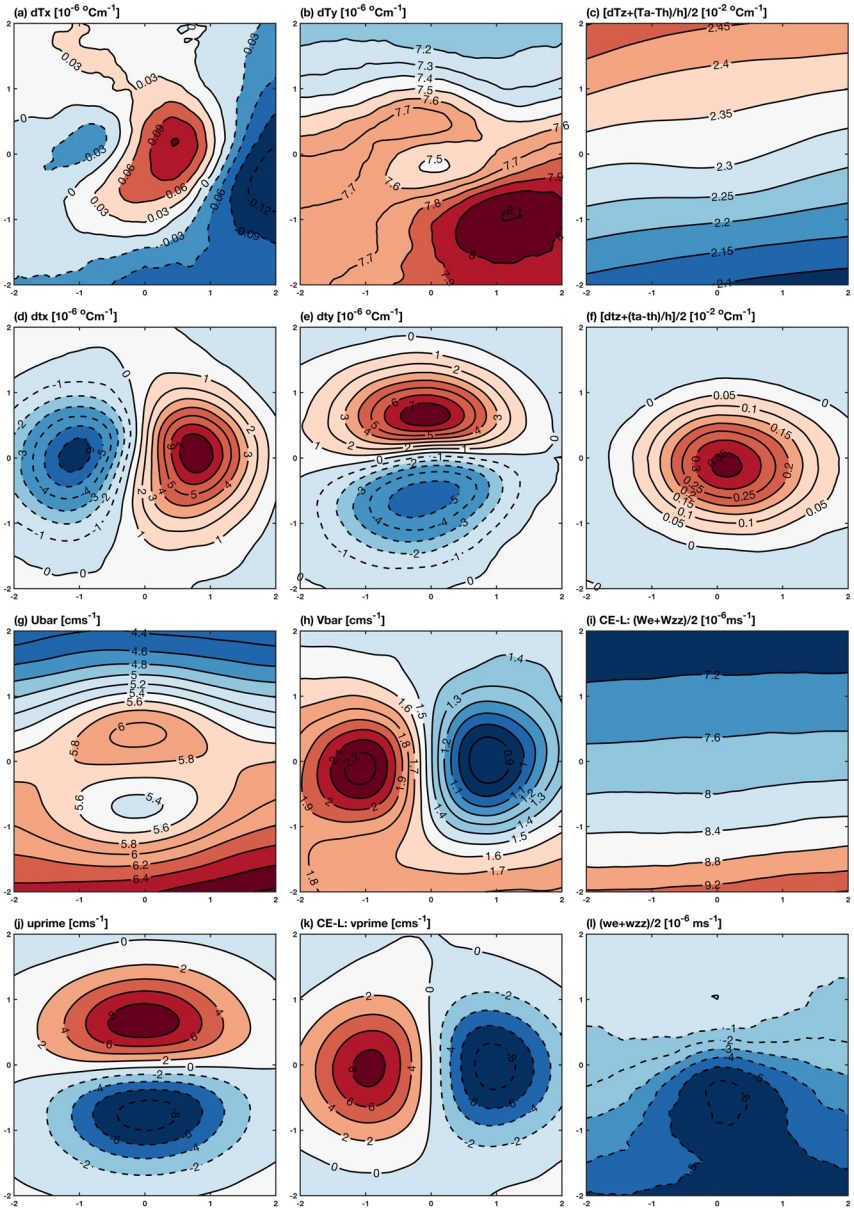

Figure 12. Climatological temperature gradient (dashed contours for negative) of CEs in the mixed layer in southern regions (30°S–50°S) of the SA in (a) zonal, $\overline{T}_x$, (b) meridional, $\overline{T}_y$, and (c) vertical, $\overline{T}_z$. Anomalous temperature gradient in (d) zonal, $T_x^{'}$, (e) meridional, $T_y^{'}$, and (f) vertical, $T_z^{'}$. Climatological current in (g) zonal $\overline{u}$, (h) meridional, $\overline{v}$, and (i) vertical, $\overline{w}$. Anomalous current in (j) zonal, u', (k) meridional, v', and (l) vertical, w'. (c)I. is 0.03×10^{-6} ℃ m^{-1} in (a), 0.1×10^{-6} ℃ m^{-1} in (b), 0.05×10^{-2} ℃ m^{-1} in (c) and (f), 1.0×10^{-6} ℃ m^{-1} in (d) and (e), 0.2 cm/s in (g), 0.1 cm/s in (h), 0.4×10^{-6} ms^{-1} in (i), 2 cm/s in (j) and (k), and 1.0×10^{-6} ms^{-1} in (l).

$$H_{swirling}^{zonal}(z)=\rho_0 C_p\int_{-2R}^{2R}T'(x=0,y,z)u_g'(x=0,y,z)dx,$$

$$H_{swirling}^{meridional}(z)=\rho_0 C_p\int_{-2R}^{2R}T'(x,y=0,z)v_g'(x,y=0,z)dx,$$

$$H_{drifting}^{zonal}(z)=\rho_0 C_p\int_{-2R}^{2R}T'(x=0,y,z)u_d dx,$$

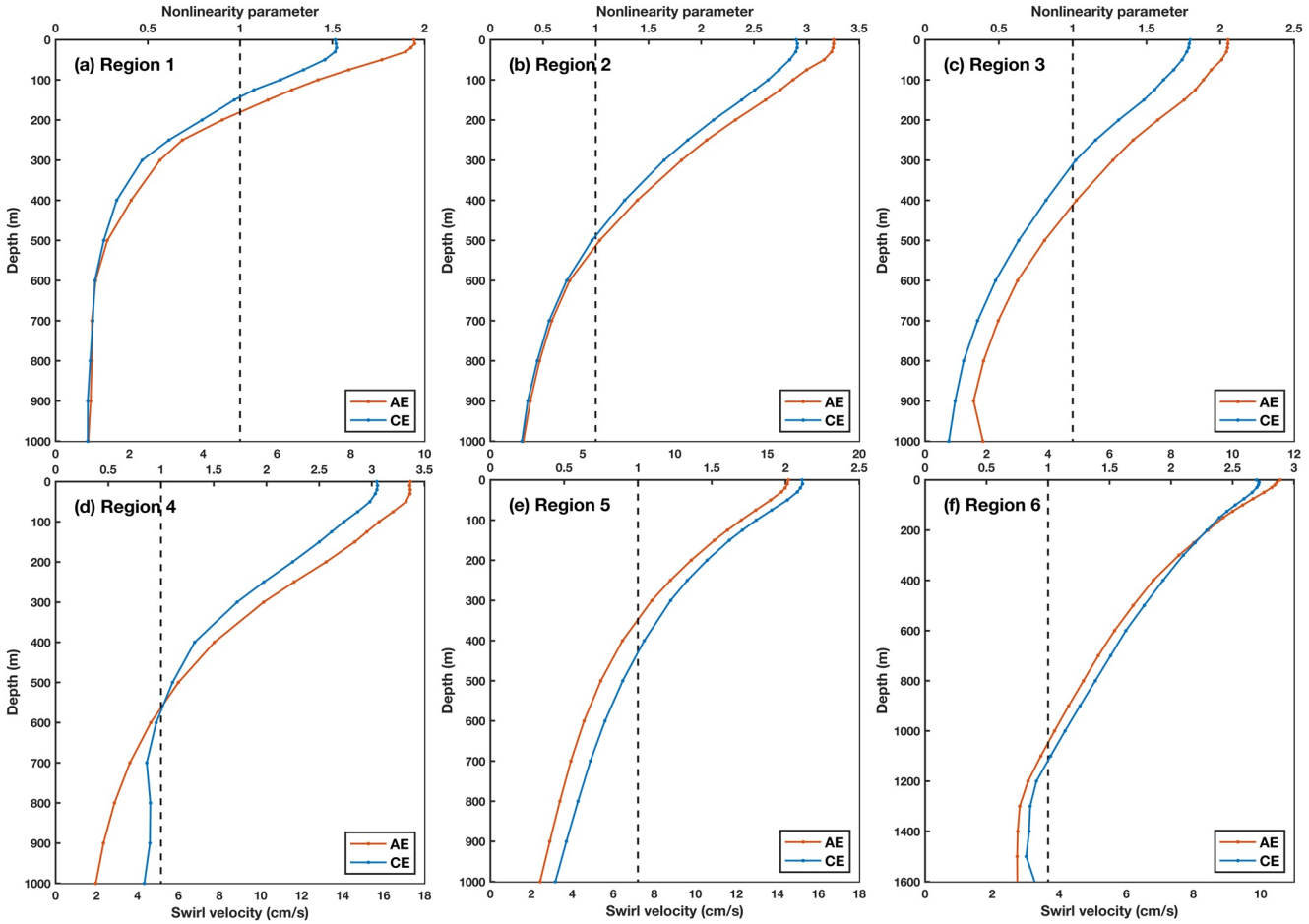

Figure 13. Vertical profiles of the swirl velocity maximum over the composite anticyclonic (red) and cyclonic (blue) eddy edges in the six sub-regions of the SA. The bottom x-axis corresponds to the swirl velocity (unit: cm/s), whereas the top x-axis corresponds to the nonlinearity parameter (ratio of the swirl velocity to the drift velocity). The trapping depths related to the vertical extent of the trapped water are estimated using a drift velocity of 5.5, 5.5, 5.0, 5.3, 7.8, and 3.5 cm/s in the six sub-regions, respectively.

$$H_{drifting}^{meridional}(z) = \rho_0 C_p \int_{-2R}^{2R} T'(x, y = 0, z) v_d dx,$$

where R is the radius of an eddy, $x = 0$ ($y = 0$) denoting the north-south (east-west) section across an eddy center, ρ_0 is the reference density of sea water, C_p is the specific capacity, is the eddy-induced temperature anomalies.

Considering the significance of poleward heat transport, we just calculate the total depth-integrated meridional heat transport as

$$H_{swirling} = \int_{D_{trap}}^{0} H_{swirl}^{meridional}(z) dz,$$

$$H_{drifting} = \int_{D_{trap}}^{0} H_{drift}^{meridional}(z) dz,$$

where D_{trap} is the eddy trapping depth (see Figure 13).

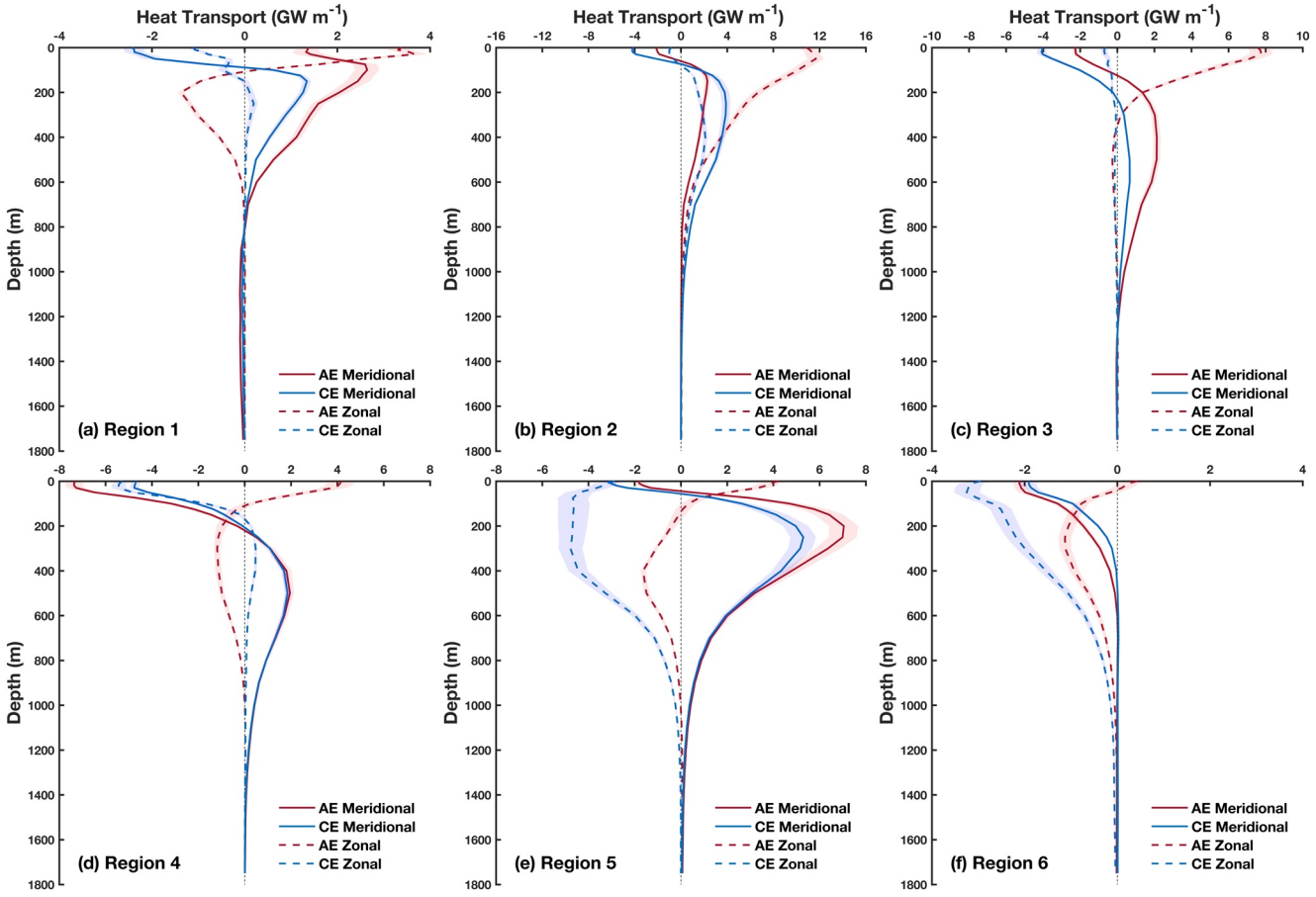

Figure 14. Composite vertical distributions of eddy-induced heat transport. The red and blue colors represent the transport by AEs and CEs, and the solid and dashed lines represent the meridional and zonal transport, respectively.

The composite vertical distributions of eddy-induced heat transport per unit depth are shown in Figure 14. A common feature for both AEs and CEs is that the heat transports are mainly concentrated above 600–1,000 m, below which the transport is much smaller as negligible. In the zonal direction (shown by the dashed curves), the maximum eastward (positive) heat transport for AEs is observed at sea surface, up to $\sim 12\, GWm^{-1}$ in the Brazil Current region (Figure 14b), and in the subsurface (200–400 m), there is maximum westward (negative) heat transport in the interior of the Subtropical gyre (Figure 14a), the AGR region (Figure 14d), the BMC zone (Figure 14e), and the northern branch of the ACC (Figure 14f). For CEs, the zonal heat transport in the upper layers above ~800 m is weaker in regions 1–3 (Figures 14a–14c). Meanwhile, the maximum westward ($\sim 6\, GWm^{-1}$) heat transport is observed at sea surface in the AGR region (Figure 14d) and the northern branch of the ACC (Figure 14f), whereas in the BMC zone (Figure 14e), the maximum westward heat transport is observed in the subsurface (~ 400 m).

In the meridional direction, the composite of eddy-induced heat transport distributes similarly for AEs and CEs, as depicted by solid curves in Figure 14. In region 1 (Figure 14a), AEs contribute to northward heat transport at all depths above 600 m and CEs contribute to southward heat transport in the upper layers above ~100 m and northward at subsurface layers. In regions 2–5 (Figures 14b–14e), both AEs and CEs contribute to southward heat transport in the upper layers above 100–200 m and northward at subsurface layers. In region 6 (Figure 14f), both AEs and CEs contribute to southward heat transport at all depths above 600 m.

The components and the total depth-integrated heat transport at each $2° \times 2°$ box are presented in Figures 15 and 16, respectively. These figures show that the meridional eddy heat transports are confined

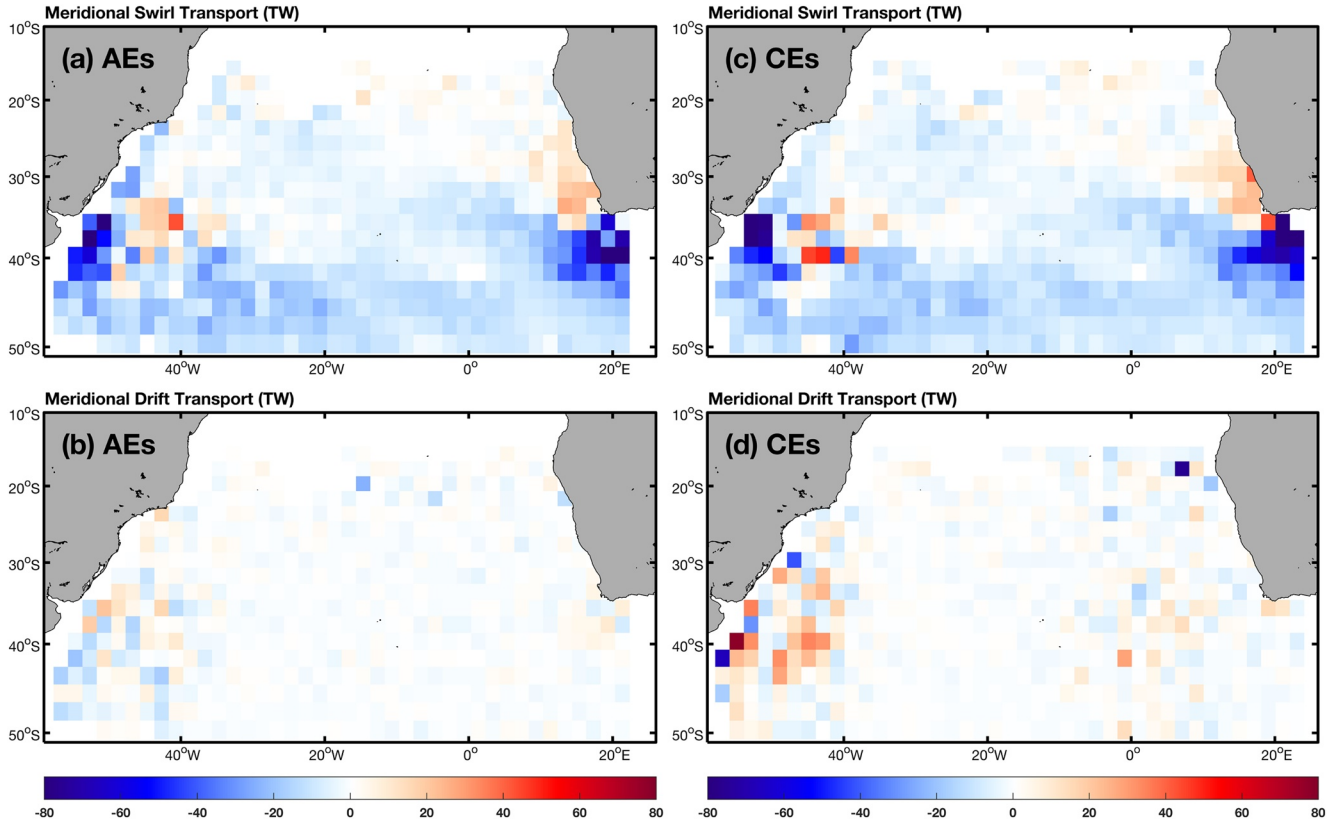

Figure 15. Components of depth-integrated meridional eddy heat transport for (a) and (c) stirring, (b) and (d) trapping induced by (a) and (b) anticyclonic and (c) and (d) cyclonic eddies. Positive and negative values denote northward and southward heat transport, respectively.

to certain latitudes and regions. Generally, the heat transport is highest in the AGR and the BMC region, where the local maximum reaches nearly ~80 TW. Figure 15 shows that the resultant trapping and stirring components of eddy meridional heat transport in the South Atlantic Ocean. It is obvious that the stirring component is larger than the trapping component. The maximum stirring heat transport with southward (northward) direction takes place in west (east) of BMC and the south (north) of AGR. In the ACC region, the stirring heat transport is poleward, whereas in a wide range of southern Atlantic Ocean (10° *S*–30° *S*), the heat transport is weak, and equatorward and poleward co-exiting. Referring to Figure 16, it demonstrates again that the total eddy transport is dominated by the stirring component. The spatial pattern of eddy heat transport is similar to one of previous studies which are estimated based on Argo profiles and satellite observations (Sun et al., 2019).

6. Summary and Discussions

In this study, we systematically explore the three-dimensional structure and heat transport characteristics of mesoscale eddies in the SA. Through analyzing the HYCOM datasets for the period of 2008–2018, we revealed that the composite horizontal structure appears dipole and monopole with a bowl-shaped vertical structure confined within different trapping depths in the major regions of the SA. By analyzing the mixed layer anomalous temperature budget, the dipole structure at low latitudes can be attributed to ocean horizontal advection, especially the meridional advection determined mainly by the combined effect of anomalous meridional current and meridional gradient of mean temperature within cyclonic eddies. The monopole structure at high latitudes can be attributed to ocean advection in which three components contribute. The zonal advection and meridional advection are the largest terms, peaking in the 1-time normalized standard eddy radius. Because of their opposite signs, the zonal and meridional advection's effect can be offset around this area. At the eddy center, the vertical advection is non-negligible. The components of

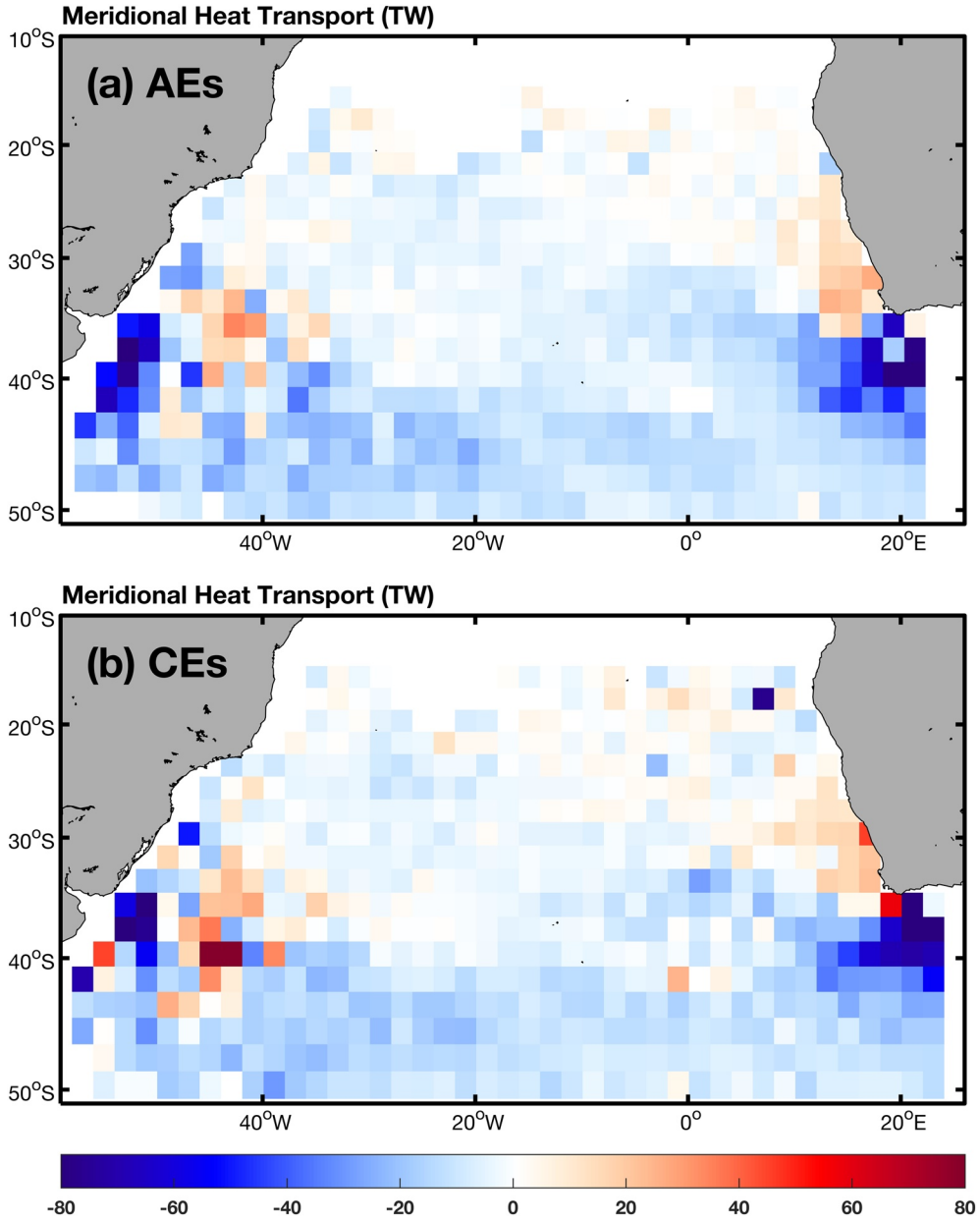

Figure 16. Horizontal distribution of depth-integrated meridional eddy heat transport (stirring + trapping) induced by (a) AEs and (b) CEs. Positive and negative values denote northward and southward heat transport, respectively.

vertical advection, including mean, anomalous, and non-linear terms in an eddy center, plays an important role in the formation of the monopole structure. To quantify the water effectively trapped and transported by the eddies, we calculate the trapping depth and estimate the swirl and drift components of eddy heat transport. The results show that the trapping depth is different in the sub-regions of the SA and the total meridional heat transport is dominated by the stirring component, and poleward in most areas, especially at high latitudes.

These results reveal that temperature anomaly structures within eddies display diverse spatial patterns in different regions of the SA, and various dynamical mechanisms play essential roles in the maintenance of those patterns. This study serves as a first step of advanced studies of the eddy structure and quantitative analysis of mixed layer heat budget over mesoscale eddies. The analysis approach may be applied to other regions and other scientific issues on mesoscale eddies. However, although we have clarified the leading

mechanisms of different spatial structures of the eddy-induced temperature anomalies in different regions of the SA, further studies are needed to explore how these eddy structures could impact on water mass property, large-scale circulation, and air-sea interactions. This would also provide useful information to validate model simulation and reanalysis products so as to further improve air-sea coupling processes in coupled general circulation models.

Data Availability Statement

The HYCOM reanalysis data sets are available at https://www.hycom.org/data/glba0pt08/expt-90pt6.

References

Amores, A., Melnichenko, O., & Maximenko, N. (2017). Coherent mesoscale eddies in the North Atlantic subtropical gyre: 3-D structure and transport with application to the salinity maximum. *Journal of Geophysical Research: Oceans*, *122*(1), 23–41. https://doi.org/10.1002/2016jc012256

Bleck, R. (2002). An oceanic general circulation model framed in hybrid isopycnic-Cartesian coordinates. *Ocean Modelling*, *4*(1), 55–88. https://doi.org/10.1016/s1463-5003(01)00012-9

Chaigneau, A., Gizolme, A., & Grados, C. (2008). Mesoscale eddies off Peru in altimeter records: Identification algorithms and eddy spatio-temporal patterns. *Progress in Oceanography*, *79*(s2–s4), 106–119. https://doi.org/10.1016/j.pocean.2008.10.013

Chaigneau, A., Le Texier, M., Eldin, G., Grados, C., & Pizarro, O. (2011). Vertical structure of mesoscale eddies in the eastern South Pacific Ocean: A composite analysis from altimetry and Argo profiling floats. *Journal of Geophysical Research*, *116*(C11), C11025. https://doi.org/10.1029/2011jc007134

Chelton, D. B., Gaube, P., Schlax, M. G., Early, J. J., & Samelson, R. M. (2011). The influence of nonlinear mesoscale eddies on near-surface oceanic chlorophyll. *Science*, *334*, 328–332. https://doi.org/10.1126/science.1208897

Chelton, D. B., Schlax, M. G., Freilich, M. H., & Milliff, R. F. (2004). Satellite measurements reveal persistent small-scale features in ocean winds. *Science*, *303*(5660), 978–983. https://doi.org/10.1126/science.1091901

Chelton, D. B., Schlax, M. G., & Samelson, R. M. (2011). Global observations of nonlinear mesoscale eddies. *Progress in Oceanography*, *91*(2), 167–216. https://doi.org/10.1016/j.pocean.2011.01.002

Chen, G., Han, W., Li, Y., McPhaden, M. J., Chen, J., Wang, W., & Wang, D. (2017). Strong intraseasonal variability of meridional currents near 5°N in the Eastern Indian Ocean: Characteristics and causes. *Journal of Physical Oceanography*, *47*(5), 979–998. https://doi.org/10.1175/jpo-d-16-0250.1

Cummings, J. A. (2005). Operational multivariate ocean data assimilation. *Quarterly Journal of the Royal Meteorological Society*, *131*(613), 3583–3604. https://doi.org/10.1256/qj.05.105

Cummings, J. A., & Smedstad, O. M. (2013). Variational data assimilation for the Global Ocean. *Data Assimilation for Atmospheric, Oceanic and Hydrologic Applications*, *II*(13), 303–343. https://doi.org/10.1007/978-3-642-35088-7_13

de Boyer Montégut, C., Madec, G., Fischer, A. S., Lazar, A., & Iudicone, D. (2004). Mixed layer depth over the global ocean: An examination of profile data and a profile-based climatology. *Journal of Geophysical Research*, *109*, C12003. https://doi.org/10.1029/2004JC002378

de Marez, C., L'Hégaret, P., Morvan, M., & Carton, X. (2019). On the 3D structure of eddies in the Arabian Sea. *Deep Sea Research Part I: Oceanographic Research Papers*, *150*, 103057. https://doi.org/10.1016/j.dsr.2019.06.003

Doglioli, A. M., Blanke, B., Speich, S., & Lapeyre, G. (2007). Tracking coherent structures in a regional ocean model with wavelet analysis: Application to Cape Basin eddies. *Journal of Geophysical Research*, *112*, C05043. https://doi.org/10.1029/2006jc003952

Dong, C., Lin, X., Liu, Y., Nencioli, F., Chao, Y., Guan, Y. ., & McWilliams, J. C. (2012). Three-dimensional oceanic eddy analysis in the Southern California Bight from a numerical product. *Journal of Geophysical Research*, *117*(C7), C00H14. https://doi.org/10.1029/2011jc007354

Dong, S., Gille, S. T., & Sprintall, J. (2007). An assessment of the Southern Ocean mixed layer heat budget. *Journal of Climate*, *20*(17), 4425–4442. https://doi.org/10.1175/jcli4259.1

Downes, S. M., Gnanadesikan, A., Griffies, S. M., & Sarmiento, J. L. (2011). Water mass exchange in the Southern Ocean in coupled climate models. *Journal of Physical Oceanography*, *41*(9), 1756–1771. https://doi.org/10.1175/2011jpo4586.1

Escudier, R., Renault, L., Pascual, A., Brasseur, P., Chelton, D., & Beuvier, J. (2016). Eddy properties in the Western Mediterranean Sea from satellite altimetry and a numerical simulation. *Journal of Geophysical Research: Oceans*, *121*, 3990–4006. https://doi.org/10.1002/2015jc011371

Faghmous, J. H., Frenger, I., Yao, Y., Warmka, R., Lindell, A., & Kumar, V. (2015). A daily global mesoscale ocean eddy dataset from satellite altimetry. *Scientific Data*, (Vol. *2*), 150028. https://doi.org/10.1038/sdata.2015.28

Ferrari, R., & Wunsch, C. (2009). Ocean circulation kinetic energy: Reservoirs, sources, and sinks. *Annual Review of Fluid Mechanics*, *41*, 253–282. https://doi.org/10.1146/annurev.fluid.40.111406.102139

Flierl, G. R. (1981). Particle motions in large-amplitude wave fields. *Geophysical & Astrophysical Fluid Dynamics*, *18*, 39–74. https://doi.org/10.1080/03091928108208773

Frenger, I., Gruber, N., Knutti, R., & Münnich, M. (2013). Imprint of Southern Ocean eddies on winds, clouds and rainfall. *Nature Geoscience*, *6*(8), 608–612. https://doi.org/10.1038/ngeo1863

Frenger, I., Münnich, M., & Gruber, N. (2018). Imprint of Southern Ocean mesoscale eddies on chlorophyll. *Biogeosciences*, *15*, 4781–4798. https://doi.org/10.5194/bg-15-4781-2018

Fu, L. L. (2006). Pathways of eddies in the South Atlantic Ocean revealed from satellite altimeter observations. *Geophysical Research Letters*, *33*(14), L14610. https://doi.org/10.1029/2006gl026245

Fu, L. L. (2009). Pattern and velocity of propagation of the global ocean eddy variability. *Journal of Geophysical Research: Oceans*, *114*(C11), C11017. https://doi.org/10.1029/2009jc005349

Garzoli, S. L., Baringer, M. O., Dong, S., Perez, R. C., & Yao, Q. (2013). South Atlantic meridional fluxes. *Deep Sea Research Part I: Oceanographic Research Papers*, *71*, 21–32. https://doi.org/10.1016/j.dsr.2012.09.003

Acknowledgments

Authors thank two anonymous reviewers for their thorough examinations and useful and helpful comments and suggestions helped improve the quality of the manuscript. This work is supported by the National Key R&D Program of China (2017YFC1404100 and 2017YFC1404104) and the National Natural Science Foundation of China (Grant No. 41775100, 41830964) as well as Shandong Province's "Taishan" Scientist Program and Qingdao "Creative and Initiative" frontier Scientist Program. This research is also supported by the Center for High Performance Computing and System Simulation, Pilot National Laboratory for Marine Science and Technology (Qingdao).

Garzoli, S. L., & Matano, R. (2011). The South Atlantic and the Atlantic meridional overturning circulation. *Deep Sea Research Part II: Topical Studies in Oceanography*, *58*(17–18), 1837–1847. https://doi.org/10.1016/j.dsr2.2010.10.063
Gaube, P., Chelton, D. B., Samelson, R. M., Schlax, M. G., & O'Neill, L. W. (2015). Satellite observations of mesoscale eddy-induced Ekman pumping. *Journal of Physical Oceanography*, *45*(1), 104–132. https://doi.org/10.1175/jpo-d-14-0032.1
Giordani, H., Caniaux, G., & Voldoire, A. (2013). Intraseasonal mixed-layer heat budget in the equatorial Atlantic during the cold tongue development in 2006. *Journal of Geophysical Research: Oceans*, *118*(2), 650–671. https://doi.org/10.1029/2012jc008280
Hausmann, U., & Czaja, A. (2012). The observed signature of mesoscale eddies in sea surface temperature and the associated heat transport. *Deep Sea Research Part I: Oceanographic Research Papers*, *70*, 60–72. https://doi.org/10.1016/j.dsr.2012.08.005
Hayes, S. P., Chang, P., & McPhaden, M. J. (1991). Variability of the sea surface temperature in the eastern equatorial Pacific during 1986-1988. *Journal of Geophysical Research*, *96*(C6), 10553–10566. https://doi.org/10.1029/91jc00942
Hu, J., Gan, J., Sun, Z., Zhu, J., & Dai, M. (2011). Observed three-dimensional structure of a cold eddy in the southwestern South China Sea. *Journal of Geophysical Research: Oceans*, *116*(C5), C05016. https://doi.org/10.1029/2010jc006810
Huang, B., Xue, Y., Zhang, D., Kumar, A., & McPhaden, M. J. (2010). The NCEP GODAS ocean analysis of the tropical Pacific mixed layer heat budget on seasonal to interannual time scales. *Journal of Climate*, *23*(18), 4901–4925. https://doi.org/10.1175/2010jcli3373.1
Ikeda, M., Mysak, L. A., & Emery, W. J. (1984). Observation and modeling of satellite-sensed meanders and eddies off Vancouver Island. *Journal of Physical Oceanography*, *14*(1), 3–21. https://doi.org/10.1175/1520-0485(1984)014<0003:oamoss>2.0.co;2
Jensen, T. G., Shulman, I., Wijesekera, H. W., Anderson, S., & Ladner, S. (2018). Submesoscale features and their interaction with fronts and internal tides in a high-resolution coupled atmosphere-ocean-wave model of the Bay of Bengal. *Ocean Dynamics*, *68*(3), 391–410. https://doi.org/10.1007/s10236-018-1136-x
Jerlov, N. G. (1968). *Optical oceanography*. Elsevier.
Jones, J. H. (1973). Vertical mixing in the Equatorial Undercurrent. *Journal of Physical Oceanography*, *1*, 241–248. https://doi.org/10.1175/1520-0485(1973)003<0286:VMITEU>2.0.CO;2
Jullion, L., Heywood, K. J., Naveira Garabato, A. C., & Stevens, D. P. (2010). Circulation and water mass modification in the Brazil-Malvinas confluence. *Journal of Physical Oceanography*, *40*(5), 845–864. https://doi.org/10.1175/2009jpo4174.1
Leyba, I. M., Saraceno, M., & Solman, S. A. (2017). Air-sea heat fluxes associated to mesoscale eddies in the Southwestern Atlantic Ocean and their dependence on different regional conditions. *Climate Dynamics*, *49*(7–8), 2491–2501. https://doi.org/10.1007/s00382-016-3460-5
Liu, Y., Yu, L., & Chen, G. (2020). Characterization of sea surface temperature and air-sea heat flux anomalies associated with mesoscale eddies in the South China Sea. *Journal of Geophysical Research: Oceans*, *125*(4), e2019JC015470. https://doi.org/10.1029/2019jc015470
Luecke, C. A., Arbic, B. K., Bassette, S. L., Richman, J. G., Shriver, J. F., Alford, M. H., et al. (2017). The global mesoscale eddy available potential energy field in models and observations. *Journal of Geophysical Research: Oceans*, *122*, 9126–9143. https://doi.org/10.1002/2017jc013136
Meijers, A. J., Bindoff, N. L., & Roberts, J. L. (2007). On the total, mean, and eddy heat and freshwater transports in the Southern Hemisphere of a ⅛° × ⅛° global ocean model. *Journal of Physical Oceanography*, *37*(2), 277–295. https://doi.org/10.1175/jpo3012.1
Melnichenko, O., Amores, A., Maximenko, N., Hacker, P., & Potemra, J. (2017). Signature of mesoscale eddies in satellite sea surface salinity data. *Journal of Geophysical Research: Oceans*, *122*(2), 1416–1424. https://doi.org/10.1002/2016jc012420
Metzger, E. J., Hurlburt, H. E., Xu, X., Shriver, J. F., Gordon, A. L., Sprintall, J., et al. (2010). Simulated and observed circulation in the Indonesian Seas: 1/12° global HYCOM and the INSTANT observations. *Dynamics of Atmospheres and Oceans*, *50*(2), 275–300. https://doi.org/10.1016/j.dynatmoce.2010.04.002
Metzger, E. J., Smedstad, O. M., Thoppil, P. G., Hurlburt, H. E., Cummings, J. A., Wallcraft, A. J., et al. (2014). US Navy operational global ocean and Arctic ice prediction systems. *Oceanography*, *27*(3), 32–43. https://doi.org/10.5670/oceanog.2014.66
Nyadjro, E. S., Subrahmanyam, B., Murty, V. S. N., & Shriver, J. F. (2012). The role of salinity on the dynamics of the Arabian Sea mini warm pool. *Journal of Geophysical Research*, *117*(C9), C09002. https://doi.org/10.1029/2012jc007978
Pacanowski, R. C., & Philander, S. G. H. (1981). Parameterization of vertical mixing in numerical models of tropical oceans. *Journal of Physical Oceanography*, *11*(11), 1443–1451. https://doi.org/10.1175/1520-0485(1981)011<1443:povmin>2.0.co;2
Qiu, B., & Chen, S. (2005). Eddy-induced heat transport in the subtropical North Pacific from Argo, TMI, and altimetry measurements. *Journal of Physical Oceanography*, *35*(4), 458–473. https://doi.org/10.1175/jpo2696.1
Qiu, B., & Chen, S. (2010). Interannual variability of the North Pacific subtropical countercurrent and its associated mesoscale eddy field. *Journal of Physical Oceanography*, *40*(1), 213–225. https://doi.org/10.1175/2009jpo4285.1
Qiu, B., Chen, S., & Schneider, N. (2017). Dynamical links between the decadal variability of the Oyashio and Kuroshio extensions. *Journal of Climate*, *30*(23), 9591–9605. https://doi.org/10.1175/jcli-d-17-0397.1
Qu, T. (2003). Mixed layer heat balance in the western North Pacific. *Journal of Geophysical Research*, *108*(C7), 3242. https://doi.org/10.1029/2002jc001536
Ren, L., & Riser, S. C. (2009). Seasonal salt budget in the northeast Pacific Ocean. *Journal of Geophysical Research: Oceans*, *114*(C12), C12004. https://doi.org/10.1029/2009jc005307
Robinson, K. (1966). An examination of Corynebacteriumspp. by gel electrophoresis. *Journal of Marine Research*, *29*, 179–184. https://doi.org/10.1111/j.1365-2672.1966.tb03465.x
Rydbeck, A. V., Jensen, T. G., & Flatau, M. (2019). Characterization of intraseasonal kelvin waves in the equatorial Pacific Ocean. *Journal of Geophysical Research: Oceans*, *124*(3), 2028–2053. https://doi.org/10.1029/2018jc014838
Schlundt, M., Brandt, P., Dengler, M., Hummels, R., Fischer, T., Bumke, K., et al. (2014). Mixed layer heat and salinity budgets during the onset of the 2011 Atlantic cold tongue. *Journal of Geophysical Research: Oceans*, *119*(11), 7882–7910. https://doi.org/10.1002/2014jc010021
Sloyan, B. M., & Rintoul, S. R. (2000). Estimates of area-averaged diapycnal fluxes from basin-scale budgets. *Journal of Physical Oceanography*, *30*(9), 2320–2341. https://doi.org/10.1175/1520-0485(2000)030<2320:eoaadf>2.0.co;2
Souza, J. M. A. C., de Boyer Montégut, C., & Le Traon, P. Y. (2011). Comparison between three implementations of automatic identification algorithms for the quantification and characterization of mesoscale eddies in the South Atlantic Ocean. *Ocean Science*, *7*(3), 317–334. https://doi.org/10.5194/os-7-317-2011
Stevenson, J. W., & Niiler, P. P. (1983). Upper ocean heat budget during the Hawaii-to-Tahiti shuttle experiment. *Journal of Physical Oceanography*, *13*(10), 1894–1907. https://doi.org/10.1175/1520-0485(1983)013<1894:uohbdt>2.0.co;2
Sun, B., Liu, C., & Wang, F. (2019). Global meridional eddy heat transport inferred from Argo and altimetry observations. *Scientific Reports*, *9*, 1345. https://doi.org/10.1038/s41598-018-38069-2
Sun, W., Dong, C., Wang, R., Liu, Y., & Yu, K. (2017). Vertical structure anomalies of oceanic eddies in the Kuroshio extension region. *Journal of Geophysical Research: Oceans*, *122*(2), 1476–1496. https://doi.org/10.1002/2016jc012226

Timmermann, R., & Beckmann, A. (2004). Parameterization of vertical mixing in the Weddell Sea. *Ocean Modelling*, *6*(1), 83–100. https://doi.org/10.1016/s1463-5003(02)00061-6

Trott, C. B., Subrahmanyam, B., & Nyadjro, E. S. (2019). Influence of mesoscale features on mixed layer dynamics in the Arabian Sea. *Journal of Geophysical Research: Oceans*, *124*(5), 3361–3377. https://doi.org/10.1029/2019jc014965

Villas Bôas, A. B., Sato, O. T., Chaigneau, A., & Castelão, G. P. (2015). The signature of mesoscale eddies on the air-sea turbulent heat fluxes in the South Atlantic Ocean. *Geophysical Research Letters*, *42*(6), 1856–1862. https://doi.org/10.1002/2015gl063105

Waite, A. M., Stemmann, L., Guidi, L., Calil, P. H. R., Hogg, A. M. C., Feng, M., et al. (2016). The wineglass effect shapes particle export to the deep ocean in mesoscale eddies. *Geophysical Research Letters*, *43*(18), 9791–9800. https://doi.org/10.1002/2015gl066463

Yang, G., Yu, W., Yuan, Y., Zhao, X., Wang, F., Chen, G., et al. (2015). Characteristics, vertical structures, and heat/salt transports of mesoscale eddies in the southeastern tropical I ndian O cean. *Journal of Geophysical Research: Oceans*, *120*(10), 6733–6750. https://doi.org/10.1002/2015jc011130

Zhan, P., Krokos, G., Guo, D., & Hoteit, I. (2019). Three-dimensional signature of the red sea eddies and eddy-induced transport. *Geophysical Research Letters*, *46*(4), 2167–2177. https://doi.org/10.1029/2018gl081387

Zhang, Q., Kumar, A., Xue, Y., Wang, W., & Jin, F.-F. (2007). Analysis of the ENSO cycle in the NCEP coupled forecast model. *Journal of Climate*, *20*(7), 1265–1284. https://doi.org/10.1175/jcli4062.1

Zhang, Z., Tian, J., Qiu, B., Zhao, W., Chang, P., Wu, D., & Wan, X. (2016). Observed 3D structure, generation, and dissipation of oceanic mesoscale eddies in the South China Sea. *Scientific Reports*, *6*, 24349. https://doi.org/10.1038/srep24349

Zhang, Z., Wang, W., & Qiu, B. (2014). Oceanic mass transport by mesoscale eddies. *Science*, *345*, 322–324. https://doi.org/10.1126/science.1252418